CLUSTER DYNAMICS WITH HETDEX AT $Z < 0.5$

A Dissertation

by

STEVEN ALVARO BOADA

Submitted to the Office of Graduate and Professional Studies of
Texas A&M University
in partial fulfillment of the requirements for the degree of

DOCTOR OF PHILOSOPHY

Chair of Committee,	Casey J. Papovich
Committee Members,	Wolfgang Bangerth
	Louis Strigari
	Nicholas Suntzeff
Head of Department,	George Welch

August 2016

Major Subject: Physics and Astronomy

ABSTRACT

Lorem ipsum dolor sit amet, consectetur adipiscing elit. Integer lectus quam, condimentum quis bibendum eu, sollicitudin eget lacus. Praesent non sodales odio. Class aptent taciti sociosqu ad litora torquent per conubia nostra, per inceptos himenaeos. Nulla ac luctus sapien. Morbi cursus sapien eget lorem fermentum hendrerit. Nam ac erat dui, in cursus velit. Vivamus hendrerit porttitor nisi, ut porttitor lorem volutpat eget. In ligula ligula, euismod ut condimentum sit amet, pulvinar sit amet diam. Pellentesque interdum, ipsum ullamcorper consequat dignissim, sem arcu egestas mauris, vitae interdum sem tortor ut ante. Nunc blandit laoreet nisi, non rutrum lorem hendrerit quis. Cras nunc diam, convallis et feugiat at, auctor id libero. Nunc facilisis massa eu eros imperdiet vestibulum. Vestibulum ante ipsum primis in faucibus orci luctus et ultrices posuere cubilia Curae; Donec non velit vitae tortor blandit semper.

Etiam vitae dolor nulla. Ut eros odio, rhoncus eget placerat vitae, elementum ac ante. Proin vitae odio eu nisl pharetra mattis. Pellentesque habitant morbi tristique senectus et netus et malesuada fames ac turpis egestas. Phasellus fermentum lacus consectetur neque consequat ullamcorper. Cras blandit urna non dui consequat molestie. Curabitur viverra nibh at nisi semper faucibus. Nam egestas mauris a enim dignissim nec consectetur tortor rutrum. Mauris at nisi in est luctus congue ut mattis est. Ut pretium, mi quis elementum cursus, ante eros suscipit ligula, ut porttitor elit leo sed turpis. Nam sed dui ligula.

DEDICATION

This is an optional page. Lorem ipsum dolor sit amet, consectetur adipiscing elit. Integer lectus quam, condimentum quis bibendum eu, sollicitudin eget lacus. Praesent non sodales odio. Class aptent taciti sociosqu ad litora torquent per conubia nostra, per inceptos himenaeos. Nulla ac luctus sapien. Morbi cursus sapien eget lorem fermentum hendrerit. Nam ac erat dui, in cursus velit. Vivamus hendrerit porttitor nisi, ut porttitor lorem volutpat eget. In ligula ligula, euismod ut condimentum sit amet, pulvinar sit amet diam. Pellentesque interdum, ipsum ullamcorper consequat dignissim, sem arcu egestas mauris, vitae interdum sem tortor ut ante. Nunc blandit laoreet nisi, non rutrum lorem hendrerit quis. Cras nunc diam, convallis et feugiat at, auctor id libero. Nunc facilisis massa eu eros imperdiet vestibulum. Vestibulum ante ipsum primis in faucibus orci luctus et ultrices posuere cubilia Curae; Donec non velit vitae tortor blandit semper.

Etiam vitae dolor nulla. Ut eros odio, rhoncus eget placerat vitae, elementum ac ante. Proin vitae odio eu nisl pharetra mattis. Pellentesque habitant morbi tristique senectus et netus et malesuada fames ac turpis egestas. Phasellus fermentum lacus consectetur neque consequat ullamcorper. Cras blandit urna non dui consequat molestie. Curabitur viverra nibh at nisi semper faucibus. Nam egestas mauris a enim dignissim nec consectetur tortor rutrum. Mauris at nisi in est luctus congue ut mattis est. Ut pretium, mi quis elementum cursus, ante eros suscipit ligula, ut porttitor elit leo sed turpis. Nam sed dui ligula.

ACKNOWLEDGEMENTS

Lorem ipsum dolor sit amet, consectetur adipiscing elit. Integer lectus quam, condimentum quis bibendum eu, sollicitudin eget lacus. Praesent non sodales odio. Class aptent taciti sociosqu ad litora torquent per conubia nostra, per inceptos himenaeos. Nulla ac luctus sapien. Morbi cursus sapien eget lorem fermentum hendrerit. Nam ac erat dui, in cursus velit. Vivamus hendrerit porttitor nisi, ut porttitor lorem volutpat eget. In ligula ligula, euismod ut condimentum sit amet, pulvinar sit amet diam. Pellentesque interdum, ipsum ullamcorper consequat dignissim, sem arcu egestas mauris, vitae interdum sem tortor ut ante. Nunc blandit laoreet nisi, non rutrum lorem hendrerit quis. Cras nunc diam, convallis et feugiat at, auctor id libero. Nunc facilisis massa eu eros imperdiet vestibulum. Vestibulum ante ipsum primis in faucibus orci luctus et ultrices posuere cubilia Curae; Donec non velit vitae tortor blandit semper.

Etiam vitae dolor nulla. Ut eros odio, rhoncus eget placerat vitae, elementum ac ante. Proin vitae odio eu nisl pharetra mattis. Pellentesque habitant morbi tristique senectus et netus et malesuada fames ac turpis egestas. Phasellus fermentum lacus consectetur neque consequat ullamcorper. Cras blandit urna non dui consequat molestie. Curabitur viverra nibh at nisi semper faucibus. Nam egestas mauris a enim dignissim nec consectetur tortor rutrum. Mauris at nisi in est luctus congue ut mattis est. Ut pretium, mi quis elementum cursus, ante eros suscipit ligula, ut porttitor elit leo sed turpis. Nam sed dui ligula.

NOMENCLATURE

B/CS   Bryan/College Station

HSUS   Humane Society of the United States

P   Pressure

T   Time

TVA   Tennessee Valley Authority

TxDOT   Texas Department of Transportation

This page is optional.

TABLE OF CONTENTS

Page

LIST OF FIGURES

1. INTRODUCTION: THE IMPORTANCE OF RESEARCH

*

Clusters of galaxies form the largest bound objects in the universe, and as such their study is a cornerstone in modern day astronomy. First recognized by 19th century astronomers, their place in astronomical canon was solidified when Edwin Hubble proofed their constituent nebulae where not bound to the Milky Way (Hubble, 1926) but collections of stars similar to the Milky Way. Work to understand their nature and origin began in ernest when Hubble & Humason (1931) used the virial theorem and the galaxy velocities in the centers of the Virgo (Smith, 1936) and Coma (Zwicky, 1933) clusters to derive their masses. The immense mass derived exceeded the total stellar mass contributed by all galaxies many times over. This lead Zwicky to theorize the existence of large amounts of non-luminous matter, and coining the term "dark matter" (DM), which we still use today.

Modern astronomy gives the composition of galaxy clusters in three many parts. The galaxies themselves comprise the most obvious feature, and contain a large portion (but not the entirety) of the luminous matter (stars) in the cluster. The intracluster medium (ICM) is the space between the cluster galaxies and is composed many of ordinary matter (baryons) which are super heated to tens of thousands of kelvin. The ICM contains the bulk of the cluster's baryonic matter, and while it is very hot, it is not very dense, with a typical value of 10^{-3} particles per cubic centimeter. The majority of the cluster's mass is located in the DM halo which surrounds the cluster.

Thought to form out of the primordial density fluctuations in the very early universe, the investigation of their formation and growth began in the 1960s. Soon thereafter, the hierarchical model of structure formation (Press & Schechter, 1974; Gott & Rees, 1975; White & Rees, 1978) was introduced. It suggests the first stars and stellar clumps grew first then subsequently merged together with dark matter and other gas clumps to form the first galaxies which then continued to merge and grow into the clusters and large scale structures we see today. This accretion of smaller systems is thought to be driven by the gravity of the DM associated with the cluster. Of course, many complicated astrophysical processes are at work during cluster growth and similarly complicated theoretical models seek to explain these processes. For a detailed review of cluster formation see Kravtsov & Borgani (2012).

The number and distribution of galaxy clusters across the sky is the finger print of the cosmology imprinted on the universe at its birth. To uncover the underlying cosmology a detailed understanding of the astrophysical processes that describe the motion of constituent galaxies and their impact on the ICM is required. So, galaxy clusters stand at the intersection of cosmology and astrophysics.

1.1 Cluster Cosmology

The current concordance cosmology is a parametrization of the Big Bang cosmological model where the universe contains a cosmological constant (Λ; often referred to as dark energy) and cold dark matter (CDM). It is often characterized by six parameters; the Hubble Constant (H_0), the baryonic matter density (Ω_b), the dark matter density (Ω_c), the dark energy density (Ω_Λ); the normalization of the power spectrum (σ_8); the spectral index of the power spectrum (n_s). Galaxy clusters are sensitive probes of Ω_m, the total mass ($\Omega_b + \Omega_c$) density in the universe, through tracing the peaks in the universal matter density often referred to as the power

spectrum of matter density fluctuations or the matter power spectrum and σ_8 by the comparison of the number density of observed halos to that predicted in cosmological models.

The determination of cosmological parameters is done by comparing the number of galaxy clusters per unit mass per unit comoving volume ($n(M, z)$) to models. See Allen et al. (2011) for a comprehensive review or Murray et al. (2013) for a more practical approach. $n(M, z)$, referred to as the halo mass function (HMF) captures the number evolution through a function which defines the particular model used. Early work by Press & Schechter (1974) and Bond et al. (1991) which assumed spherical halos, have largely been replaced by more modern fitting functions which, at the expense of an analytical solution, provide more accurate results when fit to simulation data. See Murray et al. (2013) for a review of the most common fitting functions used. Through this approach, the two parameters which clusters are most sensitive to, Ω_m and σ_8 are in reality measured as $\sigma_8 \Omega_m^\alpha$, where the value of α depends on the masses of the halos considered. The degeneracy is broken through the evolution of the HMF as a function of redshift.

The ΛCDM model of cosmology makes explicit predictions about the number and masses of galaxy clusters throughout the universe. Connecting these predictions to a set of, sufficiently large in size, observed clusters remains a principal problem. Specifically, the largest threat to modern, precision, cluster cosmology is not the identification of large numbers of clusters (the total number of clusters known is only going up) but the accurate recovery of galaxy cluster mass. This problem extends to both the very rich clusters (those with high mass) and, importantly, the poor clusters (those with low mass) as the relationship between galaxy cluster mass and many of the observables which trace mass is not well understood for such low mass clusters.

1.2   State of Play

As mass is not a direct observable, a lot of work is underway to characterize galaxy cluster masses with an observable feature of galaxy clusters. In this section, we will briefly touch on a few of the ways cluster mass is determined, and address any short comings the method may have. Generally, the methods fall into two distinct camps, simulation based and direct or statistical calibration. The goal is to constrain, as best possible, $P(X|M,z)$ or the probability (P) that a galaxy cluster of given mass (M) located at redshift (z) using observable parameter (X).

One could use various simulations to attempt to calibrate this observable–mass relation (e.g., Vanderlinde et al. 2010; Sehgal et al. 2011). However, the primary challenge to this method is the incomplete understanding of the baryonic physics which take place in galaxy cluster environments. While there have been (and continue to be) many improvements in the accuracy and power of simulations it is doubtful that in the coming years they will reach the accuracy level required to the point where the observable–mass relation is dominated only by statistics (Weinberg et al., 2013).

The second broad camp is the direct calibration of cluster masses. This recipe has two distinct but not always independent tracks. The "direct" method uses the direct observations of a small set of clusters and then uses known mass estimators, X-ray hydrostatic or weak lensing (WL) as examples, which provide a "true" mass. This directly calibrates the observable–mass relation which is then applied to a much larger sample. The complications lie in that the "true" masses are in fact estimations, and the methods used to recover these masses are subject to their own limitations. X-ray hydrostatic estimations assume hydrostatic equilibrium (e.g., Mantz et al. 2015) which may only be valid for a very small number and range

of cluster masses. The Sunyaev–Zeldovich (SZ; Sunyaev & Zeldovich 1972) effect, which uses the up–scattering of cosmic microwave background (CMB) photons to estimate cluster masses, provides accurate estimations of mass, but the ability to detect low mass galaxy clusters is currently limited by technology (e.g., Carlstrom et al. 2002). WL estimates are, in principle, correct in the mean, but they suffer from signal-to-noise requirements, limiting their usefulness in low mass clusters, and potentially suffer from line-of-sight effects as the effect is sensitive to all mass along the line of sight. Virial mass estimators which determine the cluster mass based on the motions of the member galaxies is promising in that it is a direct measurement of the depth of clusters potential well, but suffers from systematics due to cluster formation physics which disrupts the velocity field.

The statistical method of determining galaxy cluster mass relies not on direct measurements of individual clusters but the calibration of observables for the entire sample which correlate with cluster mass. One example is the spatial clustering of the galaxy clusters themselves. See Weinberg et al. (2013) for a comprehensive review. In practice, it will be a combination of the three methods touched on that will provide the most reliable determination of cluster masses.

Virial mass estimators, specifically, can be applied in both a direct and statistical fashion. Currently, the accuracy of such a method, especially to the level required for today's precision cosmology, is not well constrained. In the coming years large spectroscopic surveys will provide enough coverage, and so these methods warrant further investigation (e.g., Saro et al. 2013).

1.3   Cluster Surveys in the near-future

In the coming years, many large surveys will add further statistical advantages to the determination of cosmological parameters using galaxy clusters. At their com-

pletion, the South Pole Telescope (SPT; Carlstrom et al. 2011) and the Atacama Cosmology Telescope (ACT; Swetz et al. 2011) are expected to find approximately one thousand clusters using observations in the millimeter combined with the SZ effect. Attempts are already underway to calibrate these observations using subsamples of clusters (approximately 100 cluster candidates and 60 clusters respectively) and other observables such as virial estimates or X-ray temperature measurements (e.g., Sifón et al. 2013; Bocquet et al. 2015).

X-ray identified clusters, up until today, have mostly been observed fortuitously through targeted *Chandra* or *XMM-Newton* observations. That is soon to change with the *eROSITA* telescope onboard the Spektrum-Roentgen-Gamma Mission, which will perform an all–sky survey during its four year mission and detect an estimated 50,000 or more clusters.

Large optical surveys such as the Dark Energy Survey (DES; The Dark Energy Survey Collaboration 2005) and the Large Synoptic Survey Telescope (LSST) will survey enormous portions of the sky extremely deeply and will identify vast numbers of clusters using optical selection methods (e.g., Rykoff et al. 2014; Rozo & Rykoff 2014). However, the majority of these surveys will be photometric, and any spectral information will be obtained from preexisting datasets. And while it is possible to estimate cluster masses using photometric redshifts, primarily through the richness–mass relation, (e.g., Rykoff et al. 2012, 2014), spectroscopic followup is required to both better calibrate the relation and to obtain the level of precision needed to compete with other mass estimators.

1.3.1 Impact of This Work

As the sample of known clusters grows to many tens of thousands, spectroscopic followup becomes unfeasible. Large spectroscopic surveys will be required to reduce

systematics to a level that will allow accurate mass estimations using virial methods. The Hobby Eberly Dark Energy Experiment (HETDEX; Hill et al. 2008b) is a forthcoming blind spectroscopic survey that could potentially be used to accurately calibrate the observable–mass relation for a significant number of galaxy clusters at both extremes of the mass scale. HETDEX is designed to measure the dark energy equation of state at $z \sim 2$, and so the applicability to galaxy cluster science has not yet been investigated.

Given how much progress could be made with HETDEX, this work seeks to address this issue in two ways. First, using a set of state-of-the-art simulations we will simulate the observing strategy of HETDEX to determine the number and nature of clusters that might be observed. See Section **??**. This is done in four distinct ways and in each part we will measure the dynamical properties, such as redshift, LOSVD, and mass of the clusters. First we will use targeted observations and perfect knowledge of the observed galaxy clusters, which includes center, membership, and number to recover the desired properties. Secondly, we will assume that we know the location but not the center, membership, or number of constituent galaxies. Then we will employ the HETDEX observing strategy, including realistic pointing pattern, observational magnitude constraints, and spectral sensitivity limits to generate a set of realistic observations which are then used with perfect and less than perfect knowledge scenarios to determine the cluster properties.

In all cases, we will attempt to characterize the observable–mass relation (or relations) to better understand the dominate sources of uncertainty when using HETDEX like observations. This will enable us to more fully understand and constrain the HMF which, in turns, allows us to make more accurate measurements of the cosmological parameters traced by galaxy clusters.

The second effort of this work, outlined in Section **??**, will use targeted spectro-

scopic observations of ten nearby clusters with the Mitchell Spectrograph (formerly known as VIRUS-P; Hill et al. 2008a), an integral field unit (IFU) in a square array of 246 4.24″ diameter optical fibers, to test some of the methods used in the first method. This will provide insight in how the observable–mass relation may be improved through followup observations of targeted clusters.

2. SIMULATED PERFORMANCE, MASS RECOVERY, AND LIMITS TO COSMOLOGY

2.1 Introduction

Our ability to perform precision cosmology with clusters of galaxies has reached a critical turning point. The widely accepted ΛCDM model of cosmology makes explicit predictions about the number and masses of galaxy clusters throughout the universe. However, connecting these predictions to a set of, sufficiently large in size, observed clusters remains a principal problem. Specifically, the largest threat to modern, precision, cluster cosmology is not the identification of large numbers of clusters (the total number of clusters known is only going up) but the accurate recovery of galaxy cluster mass (e.g., Sehgal et al. 2011; Planck Collaboration 2013; Bocquet et al. 2015).

As mass is not a direct observable, a lot of work is underway to characterize galaxy cluster masses with an observable feature of galaxy clusters. The goal is to constrain, as best possible, $P(M|z,X)$ the probability (P) that a galaxy cluster of given mass (M), located at redshift (z) determined using observable parameter (X). Generally, cluster mass calibrations fall into two distinct camps, simulation based and direct or statistical calibration.

One could use various simulations to attempt to calibrate this observable–mass relation (e.g., Vanderlinde et al. 2010; Sehgal et al. 2011). However, the primary challenge to this method is the incomplete understanding of the baryonic physics which take place in galaxy cluster environments. While there have been (and continue to be) many improvements in the accuracy and power of simulations it is doubtful that in the coming years they will reach the accuracy level required where

the observable–mass relation is dominated only by statistics (Weinberg et al., 2013).

The second broad camp is the direct calibration of cluster masses. This recipe has two distinct but not always independent tracks. The "direct" method uses direct observations of a small set of clusters and then uses known mass estimators, X-ray temperatures and luminosities (e.g., Mantz et al. 2010; Rykoff et al. 2014), cosmic microwave background (CMB) observations (e.g., Vanderlinde et al. 2010; Sehgal et al. 2011), optical richness (e.g., Abell 1958; Rykoff et al. 2012) or weak lensing (WL; e.g. Rozo et al. 2010) as examples, which provide a "true" mass. This directly calibrates the observable–mass relation which is then applied to a much larger sample. The complications lie in that the "true" masses are, in fact, estimations, and the methods used to recover these cluster masses are subject to their own limitations. X-ray based cluster masses assume hydrostatic equilibrium (e.g., Mantz et al. 2015) which may only be valid for a very small number and range of cluster masses. The Sunyaev–Zel'dovich Effect (SZE; Sunyaev & Zeldovich 1972), which uses the up–scattering of CMB photons to estimate cluster masses, provides accurate estimations of mass, but the ability to detect low mass galaxy clusters is currently limited by technology (e.g., Carlstrom et al. 2002). WL estimates are, in principle, correct in the mean, but they suffer from signal-to-noise requirements, limiting their usefulness in low mass clusters, and potentially suffer from line-of-sight effects as WL is sensitive to all mass along the line-of-sight. Virial mass estimators which determine the cluster mass based on the motions of the member galaxies (e.g., Ruel et al. 2014; Sifón et al. 2015a) are promising in that it is a direct measurement of the depth of clusters potential well, but suffers from systematics due to cluster formation physics which disrupts the velocity field.

The statistical method of determining galaxy cluster mass relies not on direct measurements of individual clusters but the calibration of observables for the entire

sample which correlate with cluster mass. One example is the spatial clustering of the galaxy clusters themselves (e.g., Baxter et al. 2016). See Weinberg et al. (2013) for a comprehensive review. In practice, it will be a combination of the three methods touched on that will provide the most reliable determination of cluster masses.

Large-area sky surveys, both on going and planned, are revolutionizing cluster cosmology using a large range of wavelengths. The South Pole Telescope (SPT; Carl-strom et al. 2011) and the Atacama Cosmology Telescope (ACT; Swetz et al. 2011) are discovering many clusters through the SZE. Optically, the on going Dark Energy Survey (DES; The Dark Energy Survey Collaboration 2005) and planned Large Synoptic Survey Telescope (LSST; LSST Dark Energy Science Collaboration 2012) will identify many thousands of clusters to much lower masses than is possible with SZE measurements. However, regardless of the discovery method used, spectroscopic followup is needed to further constrain $P(M|z, X)$. But as the cluster dataset grows to many tens of thousands of clusters individual followup becomes increasingly impractical. Therefore, large spectroscopic surveys are needed to more fully constrain the observable–mass relation of clusters.

The Hobby Eberly Telescope Dark Energy eXperiment (HETDEX; Hill et al. 2008b) is a trailblazing effort to observe high-redshift large scale structures using cutting edge wide-field integral field unit (IFU) spectrographs. Designed to probe the evolution of the dark energy equation of state etched onto high redshift ($z > 2$) galaxies by the Baryon Acoustic Oscillations (BAO) (Eisenstein et al., 2005) in the first moments of the universe, the survey will observe two fields for a total of 420 degree^2 (300 degree^2, Spring field and 120 degree^2, Fall field). Tuned to find Lyα emitting (LAE) galaxies at $1.9 < z < 3.5$, HETDEX expects to find 800,000 LAEs, and more than one million [O II] emitting galaxies at $z < 0.5$ masquerading as high-redshift galaxies (Acquaviva et al., 2014).

While a large portion of the $\sim 10^6$ interloping [O $\textsc{ii}$] galaxies will be field (not associated with a bound structure) galaxies, the large area covered by HETDEX is expected to contain as many as 50 Virgo-sized ($M_{dyn} > 10^{15}$ M$_\odot$) clusters at $z < 0.5$. The near-complete spectroscopic coverage allows an unprecedentedly detailed look at a very large number of clusters ranging from group scales to the very massive. In addition to the recovery of accurate dynamical masses, detailed investigations of the of dynamical state of the clusters is possible.

Connecting the dynamical properties derived from spectroscopy to the properties inferred from other studies insures the greatest impact on future work. HETDEX overlaps with the Sloan Digital Sky Survey (SDSS; Blanton et al. 2001), SDSS stripe 82 (Annis et al., 2014), DES, the *Spitzer*/HETDEX Exploratory Large-Area Survey (SHELA; Papovich et al. 2016), and the *Spitzer* IRAC Equatorial Survey (SpIES; Timlin et al. 2016, ApJ, submitted). While the potential dataset is very rich, two large issues remain.

It is unclear how a blind spectroscopic survey with an IFU will effect the recovery of galaxy cluster dynamical properties. Unlike many previous large cluster surveys (e.g., Milvang-Jensen et al. 2008; Robotham et al. 2011; Sifón et al. 2015a) which use multi-object spectrographs, the Visible Integral-Field Replicable Unit Spectrograph (VIRUS; Hill et al. 2012) used by HETDEX samples the sky in a uniform but sparse way which could excluded member galaxies which would otherwise be included. Secondly, it is not straightforward to use spectroscopic redshifts predominately from emission-line galaxies to interpret the kinematic and dynamical states of the clusters.

This work plans to address these concerns in the following ways. We create and evaluate a HETDEX like selection "function" of galaxies over a similarly large portion of the sky and use well adopted techniques to recover the dynamical properties,

such as velocity dispersion and cluster mass. We compare these results to a series of targeted galaxy cluster observations, where each member galaxy is assumed to be observed. Each of these observations use realistic uncertainties from galaxy magnitude and line-flux limits. These strategies will better allow future work to predict the number and types of galaxy clusters which should be observed with VIRUS during both the HETDEX survey portion and through targeted follow up observations.

We begin in Section 2.2 by giving an overview of what data is used, how it is created, and how we make our "observations." Details about the determination of cluster parameters, velocity dispersion, total mass, etc., are discussed in Section 2.3. Next, we present the results of our study in Section 3.6 and discuss their implications in Section 3.7. Finally we summarize our findings in Section 3.8. A followup to this work (Boada, 2016b) will investigate how the techniques developed here will work in practice.

Throughout this paper, we adopt the following cosmological model: $\Omega_\Lambda = 0.714$, $\Omega_M = 0.286$, $\sigma_8 = 0.82$ and $H_0 = 70$ km s^{-1}Mpc^{-1}(taken from the Buzzard catalogs; see below), assume a Chabrier initial mass function (IMF; Chabrier 2003), and use AB magnitudes (Oke, 1974).

2.2   Data and Mock Observations

In this section, we describe the data products and the techniques used to replicate the HETDEX survey. We use the information from a large mock galaxy catalog supplemented by galaxies from the SDSS to create a realistic "sky" and "observe" it with a HETDEX-like observing strategy.

2.2.1   The Buzzard Mock Catalogs

The Buzzard mock galaxy catalogs (R. Wechsler et al., private communication) cover 398.49 degree^2 between $4^h < RA < 6^h$ and $-61° < DEC < -41°$ and are de-
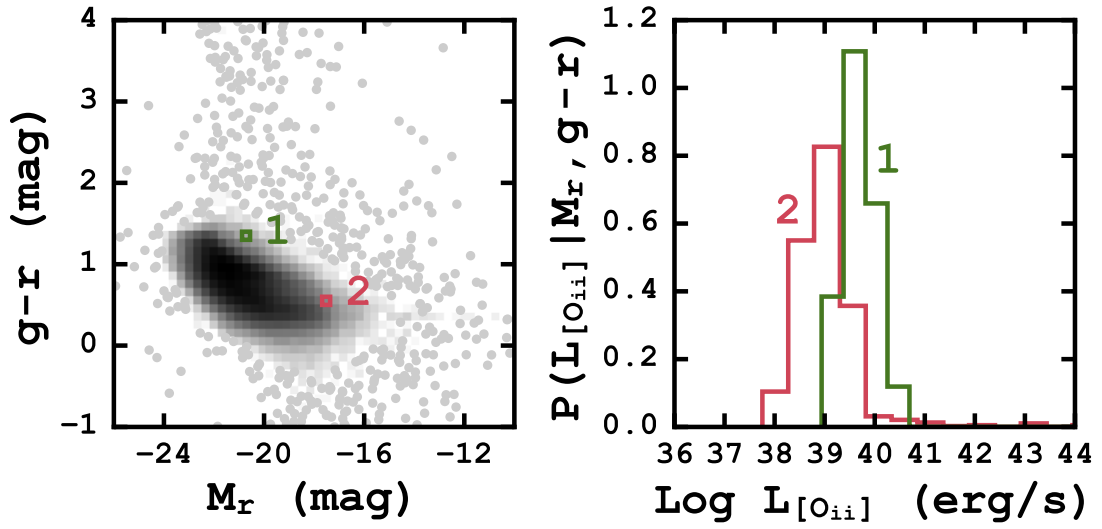
Figure 2.1: *Left*: CMD of 503113 $z < 0.2$ galaxies take from the SDSS DR12 where the shading scales with the density of points. The two colored boxes show regions containing potential catalog galaxies. *Right*: Probability histograms of the Log [O II] luminosity for the SDSS galaxies located in the two highlighted regions on the right. New [O II] luminosity (and subsequently fluxes) are assigned to catalog galaxies from slice sampling the probability histogram. See the text for a full description of the process.

rived from a combination of Sub-halo Abundance Matching (ShAM) and ADDSEDs (Adding Density Dependent Spectral Energy Distributions) tied to an in house n-body cosmological simulation. A brief description of the catalog creation is described as follows. The initial conditions are generated with a second-order Lagrangian perturbation theory using 2LPTIC (Crocce et al., 2006). Dark matter (DM) n-body simulations are run using LGADGET-2 (a version of GADGET-2; Springel 2005). The DM halos are identified using the ROCKSTAR halo finder (Behroozi et al., 2013) which also calculates halo masses.

Galaxy M_r luminosities are added to the velocity peaks using ShAM (Reddick et al., 2013), and ADDSEDs assign luminosities in the other bands. A M_r-density-SED relation is created using a SDSS training set, and for each mock galaxy the SED of a randomly selected training set galaxy which has a similar M_r and density is assigned. The result is a mock catalog containing 238 million galaxies with $r < 29$ mag and $z \leq 8.7$.

The catalog information, used in this study, is broken into two large portions. The "truth" files contain the characteristics of each individual galaxy, such as right ascension (RA), declination (DEC), redshift (z), observed and rest-frame magnitudes, and many others. The "halo" files contain information for individual halos, to which many individual galaxies may belong. This includes five estimations of dynamical mass, RA, DEC, z, three dimensional velocity dispersion, and many others. However, the catalogs do not include information for emission lines. We supplement the catalogs by generating this information; the process is described in Section 2.2.2.

We investigate the accuracy of the halo mass distribution by comparing the cumulative number density of halos above a mass (M_{200c}) threshold to the halo mass function (HMF) of Tinker et al. (2008). We calculate the HMF at central redshifts of 0.1, 0.2, and 0.4 using HMFCALC (Murray et al., 2013) and compare it galaxies in a

redshift window of $\Delta z \pm 0.01$. We find a very good agreement between the predicted HMF and the observed distribution of clusters.

2.2.2 [O II] Luminosity

The Buzzard "truth" catalog does not provide [O II] luminosities so we must assign them empirically. We use 503113 galaxies from the SDSS Data Release 12 (Alam et al., 2015) from $z = 0.05 - 0.2$, which are selected with no redshift warning, and place each galaxy on a color-magnitude diagram (CMD) of M_r and $g - r$; see the left panel of Figure 2.1.

To assign an [O II] luminosity to each galaxy in our catalog, we place the catalog galaxies on the same CMD and select all SDSS galaxies in a small 2D $(M_r, g-r)$ bin around the galaxy. We extract all of the SDSS galaxies inside that bin and create a histogram of their [O II] luminosities, the right panel of Figure 2.1. Using a slice sampling technique (Neal, 1997) we assign the catalog galaxy an [O II] luminosity based on the distribution of SDSS galaxies extracted. For catalog galaxies which are placed on the CMD near no, or very few ($1 \leq n < 10$) galaxies we assign it zero [O II] luminosity or the mean luminosity, respectively. We find no evidence of a significant bias due to galaxies being assigned zero [O II] luminosity. For the galaxies in the Buzzard catalog, 1.3% of the galaxies brighter than $g = 22$ mag (HETDEX's detection limit) have exactly zero [O II] luminosity. Of the 1.3%, only 3.3% (0.05% of all galaxies) have $g - r < 1.5$.

The left panel of Figure 2.1 shows the CMD of all SDSS galaxies. Two potential catalog galaxies are also placed on the CMD ($M_r, g - r = -17.7,\ 0.49$ and $M_r, g - r = -21.4,\ 1.24$) and indicated by the two colored boxes. The histograms show in the Figure's right panel show the probability density histograms of the Log [O II] luminosity for the SDSS galaxies in the 2D bin around the individual catalog galaxies.
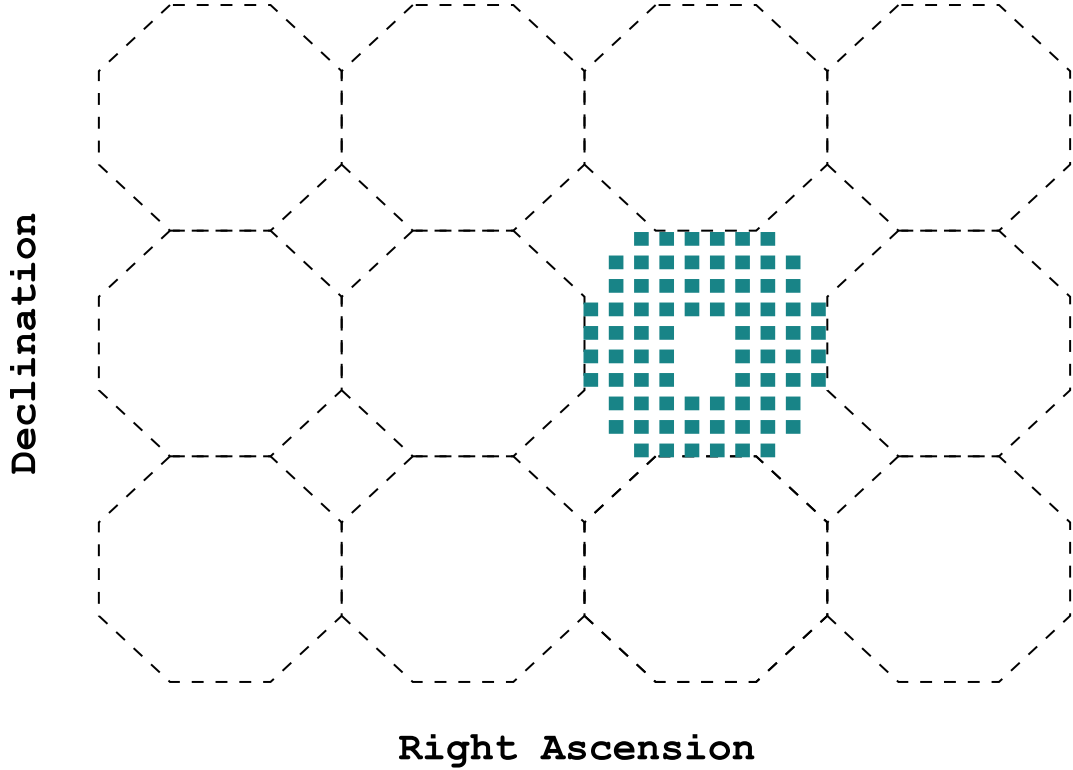
Figure 2.2: Representative observation tiling scheme for the HETDEX $16' \times 16'$ pointings. Each colored square is a single VIRUS IFU and the dashed octagons approximate the size of a single observation. See the text for more details.

We sample the distribution and assign each catalog galaxy an [O II] luminosity which is then converted into a flux.

2.2.3 Mock Observations

HETDEX will perform blind spectroscopy (R $\sim$ 750 in $3500 - 5500$ Å) over two fields along the celestial equator. The 300 degree^2, spring field and 120 degree^2 fall field will have no preselected targets. Using VIRUS on the 10-m Hobby-Eberly Telescope (Ramsey et al., 1998) the completed survey is expected to have an overall fill-factor of 1/4.5, meaning that the entire area could be covered with 4.5 dithers of

the entire survey.

The HETDEX IFU pattern is illustrated in Figure 2.2 and consists of 78 IFUs, which are comprised of 448 optical fibers subtending a $50'' \times 50''$ region on the sky (Kelz et al., 2014). The inter-IFU spacing is also $50''$ spanning a total area of $16' \times 16'$ on the sky. The individual IFUs have a fill-factor of 1/3, which will be completely filled with three dithers of the telescope at each pointing.

This means that when selecting galaxies from the Buzzard catalog we assume an observation for all galaxies laying within a colored, IFU square in Figure 2.2. Galaxies which lie between the IFUs are missed, as well as the galaxies which lie between the pointings, as there is no overlap between one pointing and the next. To cover the 398.49 degree^2 field of the Buzzard catalog we require 5370 pointings where 0.015 degree^2 of each pointing is covered by an IFU. The total area of the sky covered by an IFU is 80.80 degree^2 which gives a filling factor of 1/4.65, slightly decreased from the expected filling factor of 1/4.5.

The spectral coverage allows for the detection of [O II] ($\lambda\lambda 3727, 3729$) emitters to $z \sim 0.5$ and Ca H ($\lambda 3968.5$) and K ($\lambda 3933.7$) absorption features to $z \sim 0.4$. HETDEX is expected to detect sources with continuum brighter than $g = 22$ mag, and emission line strengths above 3.5×10^{-17} erg s^{-1} cm^{-2}.

In this work we consider two separate observing strategies, targeted and survey-like. The targeted observations use "direct" observations where each cluster is targeted individually, and every cluster member galaxy is assumed to be observed. The survey observations mimic the HETDEX observation pattern across the sky, where no cluster is directly targeted and not all cluster member galaxies are observed. Both of these observations have HETDEX-like galaxy detection thresholds, and for comparison we also include a set of targeted observations with "perfect" knowledge. Perfect observations assume no detection threshold, if a cluster member galaxy is ob-

18

served, it is also detected. This provides an important best-case scenario, and differs from the true cluster properties because the cluster properties are still calculated. These observations provide three levels of quality with "perfect knowledge" being the highest and survey being the lowest.

2.3   Recovery of Parameters

In the following sections, we outline the methods we use to derive the dynamical properties of the galaxy clusters in our sample. This is not meant to be an exhaustive study of the different methods used to recover these parameters. The following is, in many cases, a subset of the available methods to derive any single parameter. The specific choice of method may improve or diminish the accuracy of the recovered parameter, but the methods chosen were to facilitate comparison with other observational studies (e.g., Boada 2016b).

2.3.1   Cluster Redshift

The accurate determination of the cluster redshift (z_c) is crucial to the reliability of all following measurements. An incorrect cluster redshift introduces error into the measured line-of-sight velocity (LOSV) and corresponding dispersion, which, in turn, contributes to errors associated with dynamical mass and radius.

In simple terms, the cluster redshift is the mean of the redshifts of all galaxies associated with the cluster. For this work we rely on the biweight location estimator (Beers et al., 1990) because it is resistant to outlying galaxies. Although this work assumes that we know each galaxy's redshift to infinite precision, in practice, we find a simple weighted mean provides a reliable estimate of z_c when there are uncertainties on the individual galaxy redshifts.

2.3.2 Line-of-Sight Velocity Dispersion

We first calculate the LOSV to each galaxy, where

$$LOSV = c\frac{z - z_c}{1 + z_c} \tag{2.1}$$

and c is the speed of light in km s^{-1}, z is the redshift of the individual galaxy, and z_c is the overall cluster redshift described in the previous section.

The line-of-sight velocity dispersion (LOSVD) is calculated using a method of maximum likelihood following Walker et al. (2006). We maximize the probability function

$$p(\{v_1, ..., v_N\}) = \prod_{i=1}^{N} \frac{1}{\sqrt{2\pi(\sigma_i^2 + \sigma_p^2)}} \exp\left[-\frac{1}{2}\frac{(v_i - \langle u \rangle)^2}{(\sigma_i^2 + \sigma_p^2)}\right] \tag{2.2}$$

where σ_p, $\langle \mu \rangle$, and σ_i is the LOSVD, the average radial velocity and the error on the individual LOSVs respectively, using a Monte Carlo Markov Chain (MCMC) sampler (EMCEE[1]; Foreman-Mackey et al. 2013) which is based on affine-invariant ensemble sampler (see Goodman & Weare 2010 for details on affine-invariant samplers). We draw twenty thousand samples from the posterior probability distribution using simple priors, $\langle \mu \rangle$ lies between the maximum and minimum LOSV and $0 < \sigma_p < 1400$ km s^{-1}. When the full distribution of LOSVDs is not used, the final LOSVD is quoted as the median value of the posterior probability distribution with 68% error bars defined as the 16th and 84th percentiles of the same distribution.

In principle, a single statistic such as the biweight scale estimator or the gapper estimator (both from Beers et al. 1990) with many bootstrap resamplings could be used to construct a distribution of σ_p. In simple tests where the values of both σ_p and $\langle \mu \rangle$ are known. The 68% error bars derived from the MCMC method give slightly

---

[1]http://dan.iel.fm/emcee/current/

better results with the true LOSVD value bracketed by the error bars in $\sim 68\%$ of the cases versus $\sim 57\%$ with bootstrapping and a single statistic. In addition, we prefer the maximum likelihood method for its straight forward treatment of the errors in the LOSV measurements, which will become important in future observations of real clusters (e.g., Boada 2016b).

2.3.3   Dynamical Mass from Scaling Relations

The relationship between the LOSVD and cluster dynamical mass has been the focus of several studies (e.g., Evrard et al. 2008; Saro et al. 2013; Sifón et al. 2013; van der Burg et al. 2014), and a best fitting relationship for the mass enclosed by r_{200c} of the form

$$M_{200c} = \frac{10^{15}}{h(z)} \left(\frac{\sigma_{1D}}{A_{1D}} \right)^{1/\alpha} \mathrm{M}_\odot \tag{2.3}$$

with $A_{1D} = 1177 \pm 4.2$ km s^{-1} (Munari et al. 2013; referred to as σ_{15} in Evrard et al. 2008 and other works), $\alpha = 1/3$, $h(z) = H(z)/100$, and σ_{1D} is the LOSVD of the velocity tracers (dark matter particles, subhalos or galaxies). $H(z) = H_0 E(z)$ and $E(z) = \sqrt{\Omega_m(1 + z^3) + \Omega_\Lambda}$.

A growing body of work suggests that there is a significant difference in the observed LOSVD depending on the velocity tracers used. Specifically, while there is little difference between using galaxies and their host DM subhalos, there is a significant over estimation of the LOSVD when using galaxies/subhalos compared to DM particles (Munari et al., 2013). We follow other works (e.g., Kirk et al. 2015; Sifón et al. 2015b) using the scaling relation, given in Equation 3.5 from Munari et al. (2013) to facilitate comparisons with other observational studies, which rely on galaxies are tracers.

2.3.4   Other Estimates of Dynamical Mass

In this section we use two methods to predict the mass of a cluster based on other observables. Often the cluster mass is estimated based on a single observable, X-ray temperature, LOSVD, richness and others. Here we combine many observables to attempt to correct the mass inferred solely from the velocity dispersion. The first method is traditional probability based where we marginalize over a series of observables to find the most probable cluster mass. The second is based on a machine learning (ML) algorithm which attempts to "learn" the relationship between the observables and the desired output, the cluster mass. Both of these methods are examples of supervised learning algorithms where the relationship between the observable parameters and the target parameter (the cluster mass) are both known.

As with any predictive analysis it is important to test the model on data that the model has not seen before. In this section we take all of the observed clusters, our full sample, split them, and generate a training and testing set. The data is randomly split 70% training and 30% testing. We follow the ML convention and refer to the individual clusters in each set as a "sample", and the parameters associated with the cluster (z, LOSVD, mass, etc.) as "features".

2.3.4.1   Probability Based

We begin with the training sample. After selecting the desired features $\vec{x} = \{\sigma, z, ...\}$ we make the joint probability between the true cluster mass (M_{200c}) and $\vec{x}$. Figure 2.3, a corner plot, shows all of the one (marginalized probability) and two (joint probability) dimensional projections of the posterior probability distributions of the features of the training data.

The conditional probability of the mass $P(M_{200c}|\vec{x} = \{x_1, x_2, ...\})$ is determined by taking a slice through the joint probability distributions in bins centered on the

22
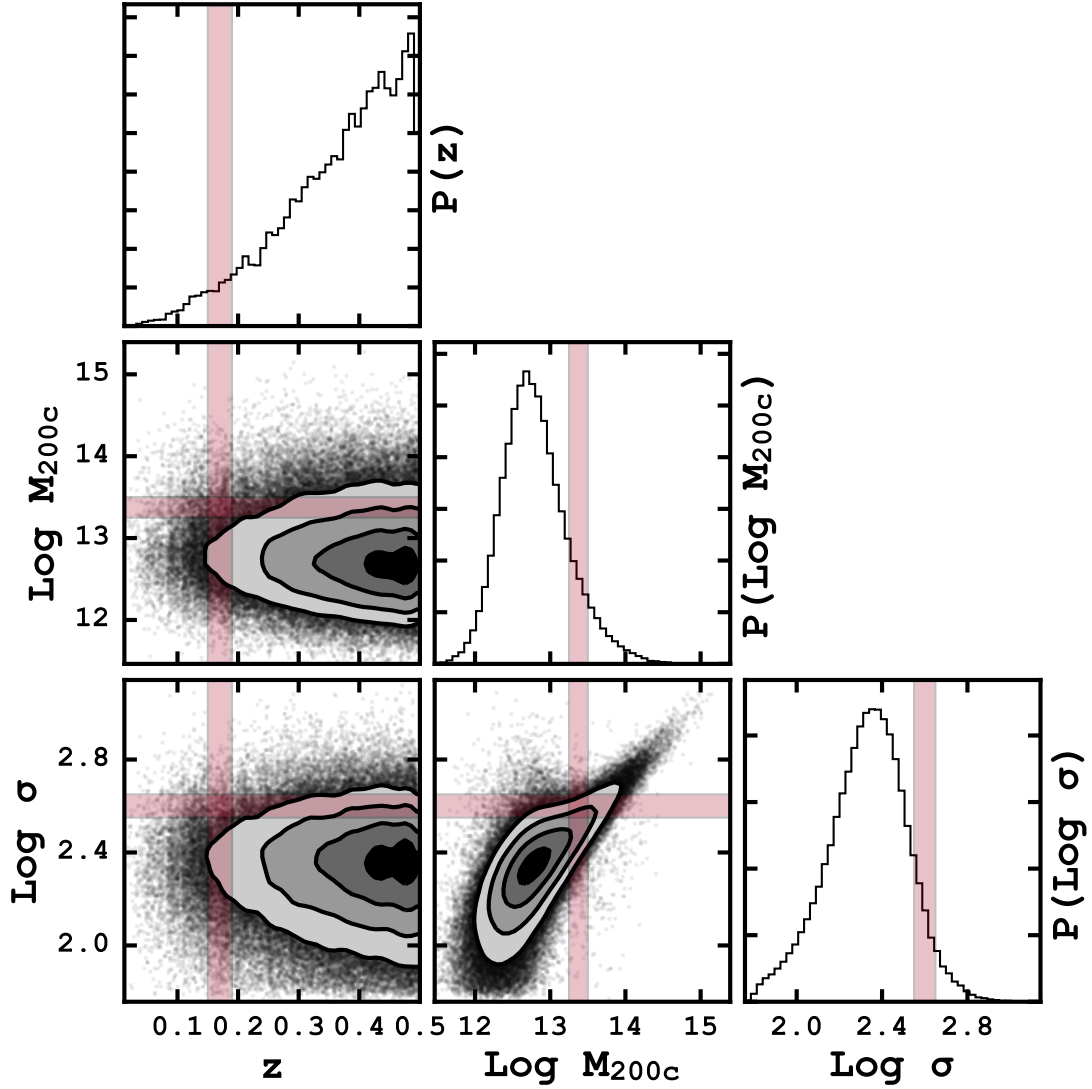
Figure 2.3: Corner plot of the *training* data with features σ and z. The corner plots shows all of the one and two dimensional posterior probability distributions used to determine the correct cluster mass. The colored rectangles, which have been enlarged for clarity, show the slices needed to create a conditional probability distribution of the mass, $P(M_{200c}|\vec{x})$. See text for a complete description.
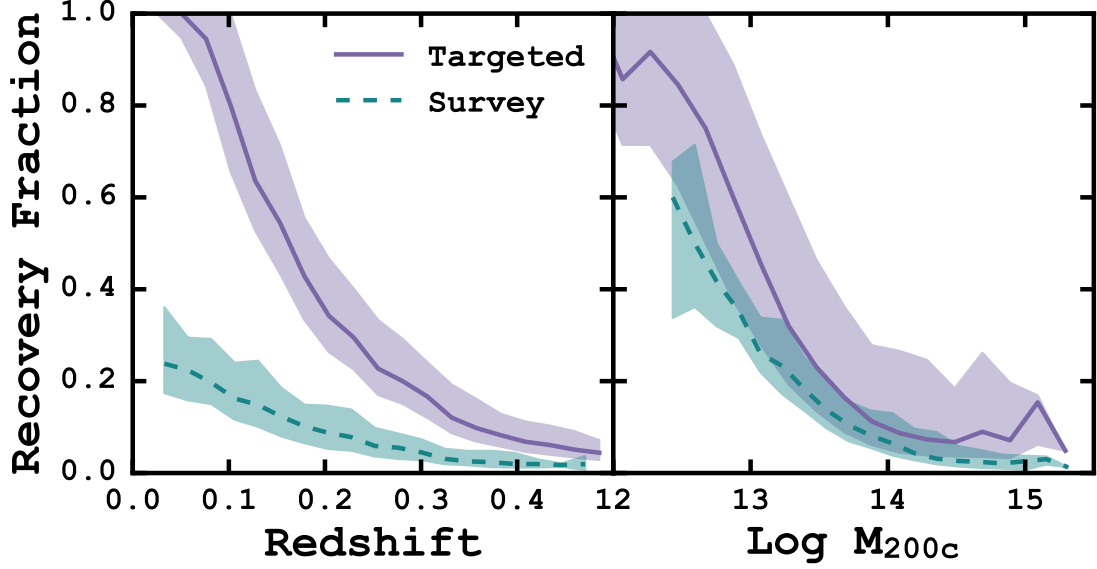
Figure 2.4: Recovery fractions (N_{obs}/N_{True}) of cluster member galaxies as a function of redshift and true cluster mass for the targeted and survey observing strategies. We have applied HETDEX-like observational limits on the cluster galaxy detection, and require at least five galaxies to be detected for a cluster to be recovered. The solid lines are the median values and the shaded regions represent the 68% scatter. The significant decline in galaxies observed with the survey strategy is due to gaps in the VIRUS IFU.

desired value. The slices, shown by the colored bars in Figure 2.3, are centered on $\sigma = 400$ km s^{-1}and $z = 0.17$. The distribution of cluster mass contained in the three dimensional bin given by the intersection of these slices is $P(M_{200c}|\vec{x} = \{\sigma = 400$km s$^{-1}, z = 0.17\})$.

For the clusters making up the *test* sample the mass is unknown (it is what we are trying to predict) but the other features are known. To determine the mass probability distribution of a test cluster, $P(M_{200c})$, we combine the conditional probability distribution, $P(M_{200c}|\vec{x})$, created previously with the probability distribution of σ

through Equation 2.4.

$$P(M_{200c}) = \int P(M_{200c}|\vec{x})P(\sigma)d\sigma \tag{2.4}$$

The expected mass is determined by calculating the first moment of the probability density. This becomes our "predicted" cluster mass, M_{pred}.

$$M_{pred} = \int M_{200c}P(M_{200c})dM_{200c} \tag{2.5}$$

The confidence interval associated with this prediction can be estimated two ways. First, by calculating the second moment of the probability density through

$$\text{Var} = \int (M_{200c} - M_{pred})^2 P(M_{200c})dM_{200c} \tag{2.6}$$

or by drawing many samples from $P(M_{200c})$ and calculating the values at the 16th and 84th percentile. In practice we find that both methods produce similar results for a large number of trials. Therefore, we quote predicted masses as the most probable mass given by Equation 2.5 and associated 68% error estimated through Equation 2.6.

2.3.4.2 Machine Learning Based

The cluster mass estimation in this section relies on a ML technique known as an ensemble method, where many estimators are created by a single learning method with the goal of improved generalization and robustness compared to a single estimation. Ensemble methods come in two general flavors. Averaging methods average (hence the name) the estimators to produce a single prediction. Boosting estimators build estimates sequentially by attempting to address poor performing estimators in

each previous step, hence "boosting" the predictive power.

Here we use an averaging ensemble learning method known as a forest of randomized decision trees often shorten to just random forest (RF). Decision trees can be visualized a flow chart where forks are the branches of the tree. The path along the tree is decided by the values of the feature(s) at each branch. RF estimators use a random subset of the training set at each fork to decide which path should be followed. The final prediction is then the average of all the final predictions from the trees. We use RF regression methods as implemented in SCIKIT-LEARN (Pedregosa et al., 2012).

Any uncertainties quoted by this method are prediction intervals not confidence intervals. A prediction interval is an estimate of the interval encompassing future observations, with a certain probability. And, unlike confidence intervals, which describe uncertainties on the different moments of a population, a prediction interval is unique to each prediction. In many regresson analyses, such as linear fitting, the prediction intervals are based on underlying assumptions of normally distributed residuals. However, RF estimators do not have any such assumptions and require special treatment.

The prediction intervals here are based on the general method of quantile regression forests (Meinshausen, 2006). The general idea is that all response variables are recorded, not just the mean. Then the prediction can be returned as the full conditional probability distribution of all responses, which allows us to generate the prediction intervals. The 68% prediction interval is determined by calculating the 16th and 84th percentile of the full conditional probability distribution.

2.4 RESULTS

Here we explore the cluster member recovery rate and mass estimates for the two observing strategies, targeted, and survey. Targeted observations are direct observations of a cluster where each cluster member galaxy, above the detection thresholds (see Section 2.2.3), is observed. Survey observations mimic the HETDEX observation strategy such that no cluster is directly observed, and only the cluster member galaxies above the detection threshold and within an IFU (see Figure 2.2) are observed. We discuss the accuracy of cluster dynamical mass derived from both the power-law scaling relation (see Equation 3.5) and through the probability and ML methods.

2.4.1 Recovery of Cluster Members

As discussed in Section 2.2.3 the observational constraints place limits on the total number of clusters member galaxies expected to be recovered. Knowing these limits will provide important information for potential future follow up or targeted observations. Figure 2.4 shows the recovery fraction of member galaxies, the number of observed galaxies divided by the number of actual galaxies (N_{obs}/N_{True}), as function of both redshift and cluster mass. It is important to note that if fewer than five member galaxies are observed ($N_{obs} < 5$) the cluster is not considered detected, and is excluded from this Figure. As expected, the targeted observing strategy where the individual clusters are targeted through several dithers to ensure near complete coverage, performs significantly better than the survey observing strategy across all redshifts and cluster masses.

For the clusters recovered as a function of redshift (left panel of Figure 2.4), there are two effects at work. The decrease in recovery fraction with increasing redshift is a magnitude effect. We check this by limiting the cluster galaxy detection by

27

absolute magnitude which increases the recovery fraction to $> 70\%$ at all redshifts, implying the decline is a result of the apparent magnitude cluster galaxy detection threshold. The second key feature is the strong decline in clusters recovered from survey observations. This is due to gaps in the VIRUS IFU. The median recovery fraction in survey observations is almost exactly 4.5 times less than the targeted median recovery fraction. As the total filling factor of the survey increases the two lines will converge.

The recovery rate as a function of cluster mass, right panel of Figure 2.4, shows that of the the low mass clusters we detect ($N_{obs} > 5$), we observe the majority of the galaxies. This also shows a rapid decrease in the detection fraction, which can again be explained by considering absolute magnitudes instead of apparent magnitudes, as above. Also, high mass clusters are rare, so in order to detect them we must probe a large volume of space. The higher redshift cluster members suffer from the limiting apparent magnitude and suppress the recovery fraction at fixed mass. If we were to limit the survey to $z < 0.2$ we find the recovery fraction of clusters, at all masses, increases substantially, and we find a much more consistent detection fraction across all masses.

2.4.2   Mass estimates

In this section we discuss the how accurately we recover the true cluster mass from a set of observations. We report on three methods, the power law based approach (Eq. 3.5), the probability based approach (Section 2.3.4.1) and the ML based method (Section 2.3.4.2). For each method we consider observations with perfect knowledge, targeted observations and survey observations.

Because it represents the best possible scenario, the perfect knowledge observations should serve as baseline to compare the probability based and ML cluster
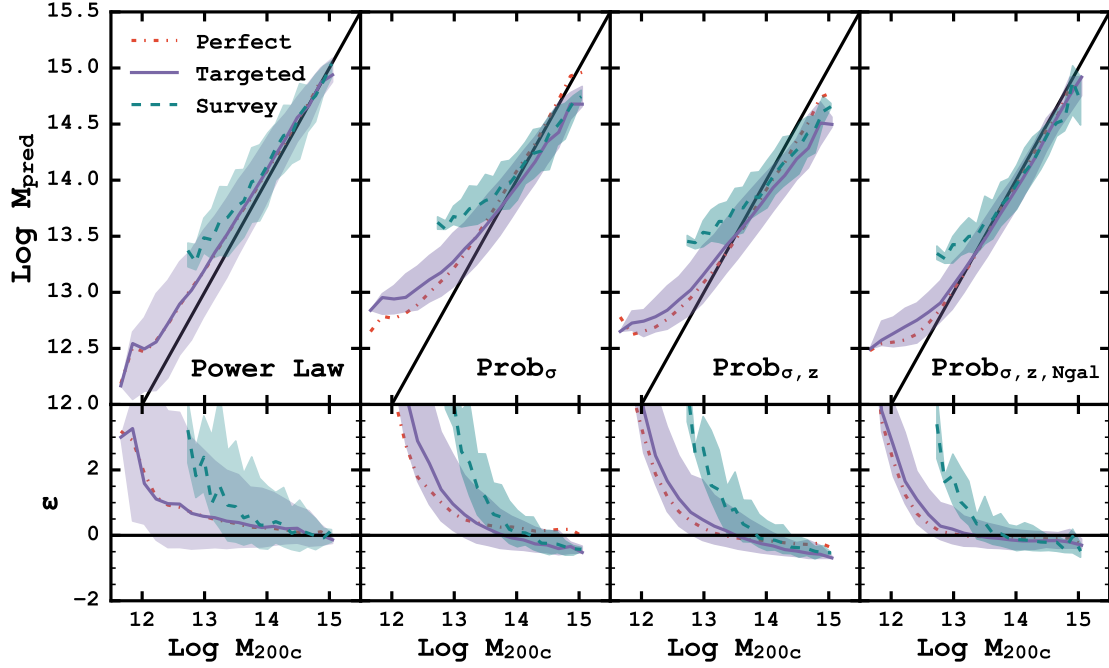
Figure 2.5: Mass predictions for the power law scaling relation (Equation 3.5) and the probability based technique with different input features as a function of true cluster mass. The bottom row of panels shows the fractional error (Equation 3.6) also as a function of true cluster mass. The solid black line shows the 1:1 relation. The solid, colored line is the median predicted mass for the targeted observing, and the colored, dashed line is the median recovered mass for the HETDEX-like observations. The shaded regions represent the 68% scatter around the median values.

mass recovery methods. And, while there are many possible metrics to evaluate performance, we compute two: the average bias (given in Table 2.1)

$$\mu_{\text{bias}}(y, \hat{y}) = \frac{1}{N} \sum_{i=0}^{N} (\hat{y}_i - y_i). \tag{2.7}$$

where y are the true values and $\hat{y}$ are the predicted values, and the scatter about the bias (given in Table 2.2)

$$\sigma_{bias}(y, \hat{y}, \mu_{bias}) = \left[\frac{1}{N-1} \sum_{i=0}^{N} (\hat{y}_i - y_i - \mu_{bias})^2 \right]^{1/2} \tag{2.8}$$

for different bins of cluster mass. Both metrics evaluate how closely the ensemble of predicted cluster masses are to the true cluster masses, and in both cases values closer to zero are better.

We begin with the perfect knowledge observations. These observations are of the same clusters as the targeted observations but without any observational limits. The cluster masses predicted by Equation 3.5 gives the following results. Across all cluster masses, we find $\mu_{bias} = 0.15 \pm 0.002$ dex and $\sigma_{bias} = 0.24 \pm 0.001$. The scatter in recovered masses can be attributed to both physical and numerical effects. The presence of any in-falling matter onto lower mass clusters can introduce a significant amount of substructure, which increases the observed LOSVD increasing the predicted mass (e.g., Ntampaka et al. 2015). Also, as the number of cluster galaxies decreases the LOSVD PDF is poorly sampled leading to poorly recovered cluster masses due to numerical effects. The cluster masses presented here are recovered using the best possible conditions, where we have perfect knowledge of the cluster membership. In reality, the mass recovery levels presented in this section represent an upper bound (the best) on the accuracy achievable through this method.

For the targeted and survey observations the power law predicted cluster masses give $\mu_{bias} = 0.13\pm0.003$ dex, $\sigma_{bias} = 0.37\pm0.002$ and $\mu_{bias} = 0.11\pm0.009$ dex, $\sigma_{bias} = 0.36\pm0.006$, respectively. So for the clusters that we detect with survey observations, we obtain similar levels of accuracy as to the targeted observations, on the average. This does not mean that the survey observations cannot be improved by targeted observations. In fact, when comparing only the galaxies which overlap between the two samples the bias and scatter of the targeted observations is significantly decreased as more cluster member galaxies are detected, better sampling the LOSVD PDF. The targeted observations performs similarly on the average because many lower mass clusters are included in the sample, increasing the bias of the overall sample.

In both Figures 2.5 and 3.4, we show the predicted (M_{pred}) versus true (M_{200c}) cluster masses for each of the two observing strategries. In each panel the solid black line is the 1:1 relationship, the solid purple line is the median recovered mass for the targeted observing, and the turquoise, dashed line is the median recovered mass for the HETDEX-like observations. The shaded regions are the 68% scatter around the median values (the 16% and 84% quartiles). For reference we also show the median masses recovered with perfect knowledge as a dash-dotted orange line. The lower panels show the fractional cluster mass error:

$$\epsilon = (M_{pred} - M_{200c})/M_{200c} \tag{2.9}$$

where M_{pred} is the predicted cluster mass and M_{200c} is the true cluster mass.

Qualitatively, the top panels of Figures 2.5 and 3.4 show that both the probability based and ML based methods out perform (closer to the black 1:1 relation) the power law method when taking advantage of other cluster observables (z, N_{gal}, etc.). Generally, we find that the single parameter probability and ML methods perform
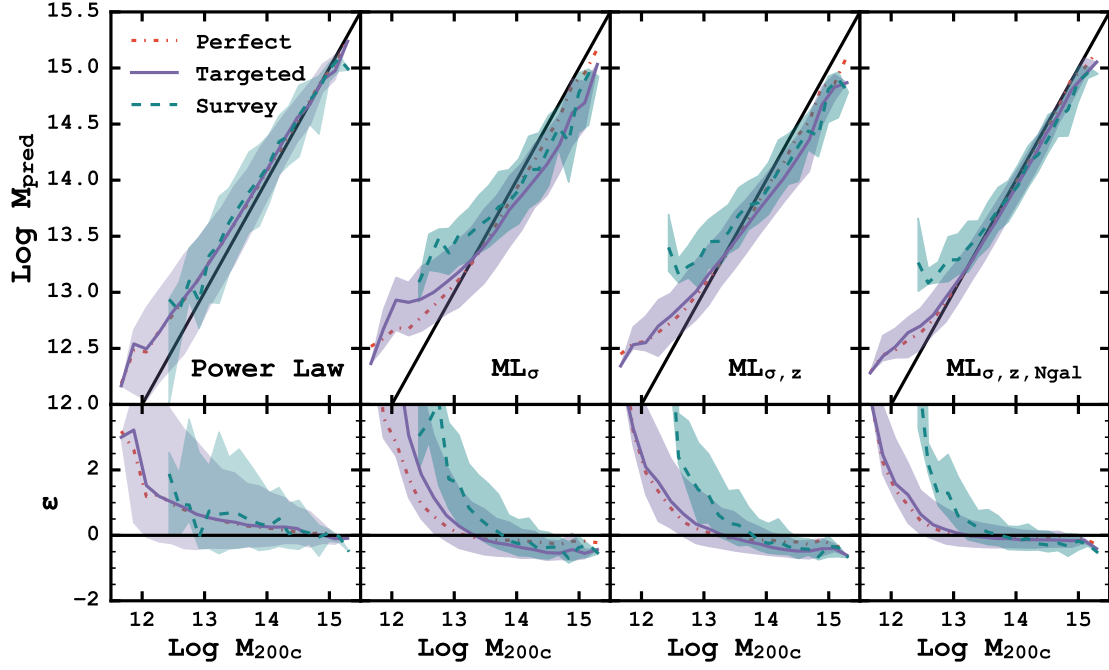
Figure 2.6: Mass predictions for the power law scaling relation (Equation 3.5) and the ML based technique with different input features as a function of true cluster mass. The bottom row of panels shows the fractional error (Equation 3.6) also as a function of true cluster mass. The solid black line shows the 1:1 relation. The solid, colored line is the median predicted mass for the targeted observing, and the colored, dashed line is the median recovered mass for the HETDEX-like observations. The shaded regions represent the 68% scatter around the median values.

significantly poorer than the power law method, especially at low cluster masses. When combined with the cluster redshift, the predicted cluster masses are improved, even though it is unclear exactly why the additional information should effect the predicted cluster mass. The final addition of the number of observed galaxies, N_{gal} acts as a type of richness estimate, and significantly improves both the bias and the amount of scatter in the predicted masses.

We quantify the bias and scatter for all of the different cluster mass recovery strategies and observing methods in Table 2.1 and Table 2.2. It should serve as a type of look up table for future cluster observations with HETDEX. The columns represent bins of predicted galaxy cluster mass and the individual values show the bias and scatter of the true cluster mass. The three horizontal sections represent perfect, targeted and survey observations respectively. So, for example, if a cluster mass is predicted using the $ML_{\sigma,z}$ method and targeted observations to be Log $M/M_\odot = 13 - 13.5$, it is biased upward by 0.03 ± 0.00 dex.

A few caveats apply to the numbers given in Table 2.1 and Table 2.2. While we provide corrections for cluster masses above 10^{15} $M_\odot$, they are estimated from only a handful of objects, and do not constitute a representative sample of clusters. On the oposite end of the cluster mass spectrum, survey observations of low mass clusters are incomplete for two potential reasons. There are very few, if any, clusters detected with survey observations below 10^{12} $M_\odot$. Missing corrections above 10^{12} $M_\odot$ in the probability based methods are due to low number statstics and an inability to sample the cluster mass PDF well enough to assign cluster mass predictions.

2.4.2.1   Significance of Cosmology Choice

The underlying simulation used to produce the Buzzard catalogs, as with every simulation, makes specific assumptions about the cosmology used and how the

Table 2.1: Mean bias (M_{pred} - M_{200c}) for different bins of predicted cluster mass. This table shows the bias in the predicted cluster mass for the perfect (top section), targeted (middle section), and survey (bottom section) observations in different predicted mass bins. The different mass recovery strategies are given in the leftmost column. It can be used to understand how the predicted cluster mass differs from the true cluster masses. Positive numbers indicate the predicted cluster mass over estimates when compared to the true cluster mass.

	Method		Bins – Log M_{pred}				
		$11.5 - 12$	$12 - 12.5$	$12.5 - 13$	$13 - 13.5$	$13.5 - 14$	$14 - 14.5$
Prob Based	Power Law	0.49 ± 0.09	0.28 ± 0.02	0.23 ± 0.01	0.16 ± 0.00	0.11 ± 0.00	0.07 ± 0.00
	σ	0.87 ± 0.04	0.53 ± 0.01	0.32 ± 0.01	0.16 ± 0.00	0.10 ± 0.00	0.07 ± 0.00
	σ, z	0.76 ± 0.04	0.42 ± 0.01	0.17 ± 0.00	0.01 ± 0.00	-0.06 ± 0.00	-0.11 ± 0.0
	σ, z, N_{gal}	0.65 ± 0.03	0.28 ± 0.01	0.04 ± 0.01	-0.02 ± 0.00	-0.02 ± 0.00	-0.05 ± 0.0
ML Based	Power Law	0.49 ± 0.09	0.28 ± 0.02	0.23 ± 0.01	0.16 ± 0.00	0.11 ± 0.00	0.07 ± 0.00
	σ	0.69 ± 0.05	0.36 ± 0.01	0.15 ± 0.01	-0.02 ± 0.00	-0.07 ± 0.00	-0.09 ± 0.0
	σ, z	0.62 ± 0.05	0.33 ± 0.01	0.12 ± 0.00	-0.01 ± 0.00	-0.06 ± 0.00	-0.09 ± 0.0
	σ, z, N_{gal}	0.51 ± 0.04	0.23 ± 0.01	0.05 ± 0.00	-0.02 ± 0.00	-0.02 ± 0.00	-0.02 ± 0.0
Prob Based	Power Law	0.49 ± 0.08	0.27 ± 0.02	0.20 ± 0.01	0.13 ± 0.01	0.10 ± 0.01	0.09 ± 0.01
	σ	1.02 ± 0.03	0.66 ± 0.01	0.40 ± 0.00	0.17 ± 0.00	0.02 ± 0.00	-0.08 ± 0.0
	σ, z	0.85 ± 0.05	0.49 ± 0.01	0.25 ± 0.00	0.08 ± 0.00	-0.06 ± 0.00	-0.21 ± 0.0
	σ, z, N_{gal}	0.70 ± 0.03	0.37 ± 0.01	0.13 ± 0.00	0.01 ± 0.00	-0.05 ± 0.00	-0.12 ± 0.0
ML Based	Power Law	0.49 ± 0.08	0.27 ± 0.02	0.20 ± 0.01	0.13 ± 0.01	0.10 ± 0.01	0.09 ± 0.01
	σ	0.76 ± 0.07	0.54 ± 0.01	0.26 ± 0.01	0.01 ± 0.00	-0.13 ± 0.00	-0.23 ± 0.0
	σ, z	0.66 ± 0.03	0.37 ± 0.01	0.17 ± 0.01	0.03 ± 0.00	-0.09 ± 0.00	-0.21 ± 0.0
	σ, z, N_{gal}	0.57 ± 0.03	0.28 ± 0.01	0.09 ± 0.00	-0.01 ± 0.00	-0.05 ± 0.00	-0.08 ± 0.0
Prob Based	Power Law	...	...	0.53 ± 0.04	0.30 ± 0.02	0.16 ± 0.01	0.07 ± 0.01
	σ	...	...	0.77 ± 0.03	0.42 ± 0.01	0.18 ± 0.01	-0.03 ± 0.0
	σ, z	...	...	0.61 ± 0.03	0.29 ± 0.01	0.08 ± 0.01	-0.11 ± 0.0
	σ, z, N_{gal}	...	...	0.48 ± 0.04	0.18 ± 0.01	0.02 ± 0.01	-0.08 ± 0.0
ML Based	Power Law	...	0.06 ± 0.46	0.17 ± 0.07	0.17 ± 0.02	0.13 ± 0.01	0.07 ± 0.01
	σ	...	0.58 ± 0.10	0.54 ± 0.04	0.24 ± 0.02	0.03 ± 0.01	-0.17 ± 0.0
	σ, z	...	1.02 ± 0.20	0.42 ± 0.04	0.19 ± 0.01	0.03 ± 0.01	-0.14 ± 0.0
	σ, z, N_{gal}	...	0.91 ± 0.26	0.39 ± 0.03	0.12 ± 0.01	-0.00 ± 0.01	-0.08 ± 0.0

galaxies are populated into the DM halos. When using simulation data to train ML methods, we incorporate all of those assumptions into the learned feature associations. This could lead to a notable bias when applying the ML method to data (real or simulated) which has significantly different cosmological assumptions.

To investigate this, we select cluster halo and galaxy catalogs from the Millennium simulation (Springel et al., 2005) obtained via querying the Millennium online database[2] (Lemson & The Virgo Consortium, 2006). The Millennium simulation tracks 2160^3 dark matter particles of 8.6×10^8 h^{-1} M$_\odot$ inside a comoving 500 $(h^{-1}\mathrm{Mpc})^3$ box from $z = 127$ to 0. It adopts a flat cosmological model based of the values derived from the Two-degree Field Galaxy Redshift Survey (Colless et al., 2001) and the first year data of the *Wilkinson Microwave Anisotropy Probe* (WMAP; Spergel et al. 2003): $\Omega_\Lambda = 0.75$, $\Omega_M = 0.25$, $\sigma_8 = 0.9$, $n_s = 1$ and $H_0 = 73$ km s^{-1}Mpc^{-1}.

The halo catalogs are created using a friends-of-friends algorithm (e.g., Turner & Gott, J. R. 1976) with linking length, $b = 0.2$. The halos are populated with galaxies using a semi-analytical model described in Croton et al. (2006); De Lucia et al. (2006); De Lucia & Blaizot (2007).

We select 4806 clusters, comprised of 623663 galaxies, at $0.02 < z < 0.5$ and $M > 10^{13}$ M$_\odot$, and apply the same data processing as with the Buzzard galaxies. We begin by assigning each galaxy an [O II] flux value (see Section 2.2.2), and "observe" each galaxy using realistic (see Section 2.2.3) observational limits. After recovering 3750 clusters which have at least five galaxies observed, we calculate the LOSVD of each cluster as in Section 2.3.2.

Cluster masses are assigned using the ML methods (see Section 2.3.4.2) using two different training sets. We use the full set of clusters detected in the Buzzard catalogs

---

[2]http://gavo.mpa-garching.mpg.de/Millennium/

35
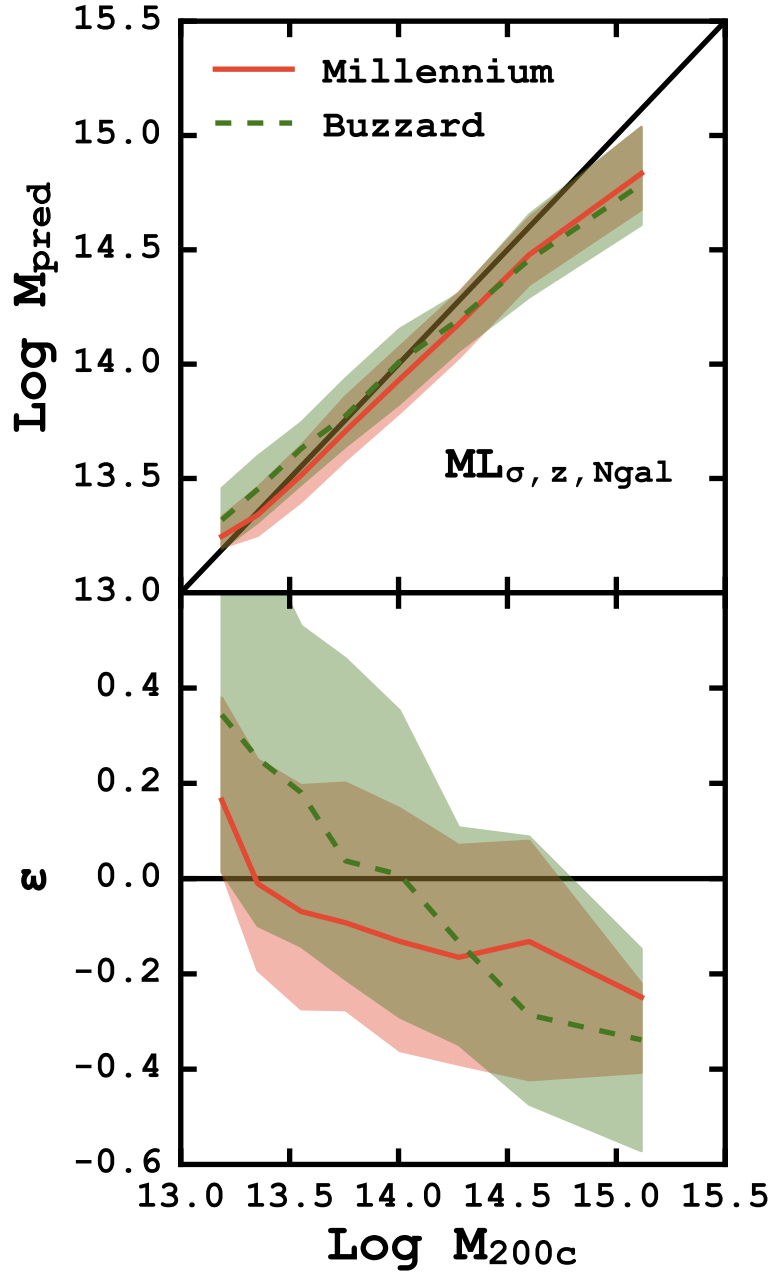
Figure 2.7: *Top:* ML based cluster mass predictions for the Millennium simulation clusters where the ML method has been trained with either a subset of the Millennium clusters (solid line) or the Buzzard catalog (dashed line). The shaded areas show the 68% scatter around the median. The solid black line shows the 1:1 relation.The solid black line shows the 1:1 relation. *Bottom:* The fractional error (Equation 3.6) also as a function of true cluster mass. The similarity of the predictions with the different training sets demonstrates how the ML method is not sensitive to the underlying cosmological assumptions.

(14000 clusters with $M > 10^{11}$ M$_\odot$) and a training-testing split of the Millennium clusters. The top panel of Figure 2.7 shows the ML predicted cluster masses as a function of true cluster mass for the $\sim$4000 Millennium clusters with the two different training sets. The median (solid and dashed lines) predicted cluster masses show similar trends regardless of the training data set used. Figure 2.7's bottom panel show the fraction error (Equation 3.6) also as a function of true cluster mass. The large amount of scatter (the shaded area) in the fractional error for the Buzzard trained predictions is due to the training set including clusters with masses below the $M = 10^{13}$ M$_\odot$ threshold for the Millennium clusters. This allows the ML method to predict masses which can be significantly different, whereas the Millennium training set does not include $M < 10^{13}$ M$_\odot$ clusters, which reduces the scatter of the predicted masses.

Based on these tests, we do not find a significant cause for concern with using trained ML methods to predict our galaxy cluster masses when the underlying cosmological choices are different. This highlights the versatility of our chosen ML method. The ML method could be further diversified by including cluster measurements from a wide range of cosmological simulations (or observations) which, in affect, marginalizes over all the cosmological assumptions further reducing the dependence.

2.5   HETDEX as a Galaxy Cluster Survey at $z < 0.5$

2.5.1   Impact on Cluster Cosmology

Galaxy clusters are sensitive probes of Ω_m, the total mass $(\Omega_b + \Omega_c)$ density in the universe, by tracing the peaks in the universal matter density often referred to as the power spectrum of matter density fluctuations or the matter power spectrum and $\sigma_8 h^{-1}$, the normalization of the power spectrum, by the comparison of the number

Table 2.2: Scatter in cluster mass after bias correction for different bins of predicted cluster mass. This table shows the scatter in the predicted cluster mass for the perfect (top section), targeted (middle section), and survey (bottom section) observations in different predicted mass bins. The different mass recovery strategies are given in the leftmost column. It can be used to understand how the predicted cluster mass differs from the true cluster masses.

| | Method | Bins – Log M_{pred} |
		$11.5 - 12$	$12 - 12.5$	$12.5 - 13$	$13 - 13.5$	$13.5 - 14$	$14 - 14.5$	
Prob Based	Power Law	0.36 ± 0.07	0.39 ± 0.01	0.34 ± 0.00	0.22 ± 0.00	0.16 ± 0.00	0.14 ± 0.00	0.
	σ	0.16 ± 0.03	0.24 ± 0.01	0.26 ± 0.00	0.20 ± 0.00	0.16 ± 0.00	0.14 ± 0.00	0.
	σ, z	0.17 ± 0.03	0.21 ± 0.01	0.23 ± 0.00	0.19 ± 0.00	0.16 ± 0.00	0.55 ± 0.01	0.
	σ, z, N_{gal}	0.10 ± 0.02	0.14 ± 0.01	0.47 ± 0.01	0.14 ± 0.00	0.10 ± 0.00	0.54 ± 0.01	1.
ML Based	Power Law	0.36 ± 0.07	0.39 ± 0.01	0.34 ± 0.00	0.22 ± 0.00	0.16 ± 0.00	0.14 ± 0.00	0.
	σ	0.22 ± 0.04	0.27 ± 0.01	0.29 ± 0.00	0.24 ± 0.00	0.21 ± 0.00	0.19 ± 0.00	0.
	σ, z	0.19 ± 0.04	0.22 ± 0.01	0.25 ± 0.00	0.20 ± 0.00	0.18 ± 0.00	0.16 ± 0.00	0.
	σ, z, N_{gal}	0.15 ± 0.03	0.18 ± 0.01	0.17 ± 0.00	0.14 ± 0.00	0.10 ± 0.00	0.08 ± 0.00	0.
Prob Based	Power Law	0.33 ± 0.07	0.41 ± 0.01	0.43 ± 0.01	0.39 ± 0.00	0.33 ± 0.00	0.27 ± 0.01	0.
	σ	0.14 ± 0.03	0.19 ± 0.01	0.24 ± 0.00	0.25 ± 0.00	0.25 ± 0.00	0.22 ± 0.00	0.
	σ, z	0.19 ± 0.04	0.20 ± 0.01	0.24 ± 0.00	0.24 ± 0.00	0.23 ± 0.00	0.56 ± 0.01	0.
	σ, z, N_{gal}	0.14 ± 0.03	0.18 ± 0.01	0.20 ± 0.00	0.19 ± 0.00	0.17 ± 0.00	0.67 ± 0.01	2.
ML Based	Power Law	0.33 ± 0.07	0.41 ± 0.01	0.43 ± 0.01	0.39 ± 0.00	0.33 ± 0.00	0.27 ± 0.01	0.
	σ	0.29 ± 0.06	0.29 ± 0.01	0.31 ± 0.00	0.31 ± 0.00	0.32 ± 0.00	0.30 ± 0.01	0.
	σ, z	0.14 ± 0.03	0.23 ± 0.01	0.26 ± 0.00	0.25 ± 0.00	0.24 ± 0.00	0.22 ± 0.00	0.
	σ, z, N_{gal}	0.13 ± 0.03	0.21 ± 0.01	0.21 ± 0.00	0.18 ± 0.00	0.16 ± 0.00	0.14 ± 0.00	0.
Prob Based	Power Law	...	...	0.16 ± 0.03	0.29 ± 0.01	0.33 ± 0.01	0.31 ± 0.01	0.
	σ	...	...	0.11 ± 0.02	0.18 ± 0.01	0.22 ± 0.01	0.22 ± 0.01	0.
	σ, z	...	...	0.13 ± 0.03	0.19 ± 0.01	0.22 ± 0.01	0.21 ± 0.01	1.
	σ, z, N_{gal}	...	...	0.14 ± 0.03	0.18 ± 0.01	0.19 ± 0.01	0.19 ± 0.01	2.
ML Based	Power Law	...	$1.41 \pm ...$	0.40 ± 0.05	0.41 ± 0.02	0.38 ± 0.01	0.32 ± 0.01	0.
	σ	...	$0.30 \pm ...$	0.27 ± 0.03	0.28 ± 0.01	0.30 ± 0.01	0.30 ± 0.01	0.
	σ, z	...	$0.61 \pm ...$	0.22 ± 0.03	0.25 ± 0.01	0.25 ± 0.01	0.25 ± 0.01	0.
	σ, z, N_{gal}	...	$0.80 \pm ...$	0.19 ± 0.02	0.21 ± 0.01	0.20 ± 0.01	0.19 ± 0.01	0.

density of observed clusters to that predicted in cosmological models. Although, in reality, one measures $\sigma_8 h^{-1} \Omega_m^q$, where the value of q depends on the masses and redshifts of the halos considered.

To get a sense of how well HETDEX will be able to constrain cosmological parameters we follow the discussion of Weinberg et al. (2013), and begin with a few simplifying assumptions. While sensitive to Ω_m, the number density of clusters do not necessarily provide the strongest contraint, so we assume that some combination of other data sets (e.g., CMB, BAO, supernovae, WL, etc.) will constrain Ω_m to higher precision than is possible with clusters alone.

To estimate the error associated with a measurement of $\sigma_8 h^{-1}$ (which Weinberg et al. 2013 refer to as $\sigma_{11,abs}$), Weinberg et al. (2013) consider two sources of uncertainty, the systematic uncertainties in cluster mass calibration and the statistical uncertainty in the observed number density of clusters. The authors combine these two uncertainties though (their Eq. 141):

$$\Delta \ln \sigma_8 h^{-1}(z) \approx q(z) \times \max \left[\Delta \ln M, \alpha(z)^{-1} \Delta \ln N \right]. \tag{2.10}$$

where q is the degeneracy exponent between $\sigma_8 h^{-1}$ and Ω_m, $\Delta \ln M$ is the mass scale uncertainty, $\Delta \ln N$ is the cluster statistical uncertainty, and α is slope of the cumulative HMF. Using the Tinker et al. (2008) HMF at $z \sim 0.2$ and a limiting cluster mass of 10^{14} M$_\odot$, Weinberg et al. (2013) estimate $q \sim 0.4$, $\alpha \sim 3$, and find that any cluster survey with more than 10-20 clusters is dominated by the uncertainty in the overall mass scale.

For a survey such as HETDEX, we can estimate the constraints on $\sigma_8 h^{-1}$ using Equation 2.10. Considering clusters with masses above 10^{14} M$_\odot$, with perfect knowledge, and the ML based cluster mass estimates the mass scale uncertainty (given in

Table 2.2) is reduced to ~ 0.075 dex or about 20%. This gives a uncertainty on $\sigma_8 h^{-1}$ of 7%. For clusters above 10^{14} $M_\odot$, survey observations can constrain the masses to about 51% which, in turn, constrains $\sigma_8 h^{-1}$ to 20%.

Because of the simplifying assumptions, and the superior quality of the data (no contamination, signal-to-noise issues, etc.), realistic expectations for HETDEX is to directly constrain $\sigma_8 h^{-1}$ to better precision than other methods (e.g., CMB, WL, X-ray) seems bleak. For example, de Haan et al. (2016) constrain $\sigma_8 h^{-1}$ to $\sim 5\%$ using a sample of 337 SZE detected clusters from the SPT-SZE survey. For the ~ 1500 clusters detected with survey observations to constrain $\sigma_8 h^{-1}$ and to be dominated by cluster statistics alone ($\Delta \ln N \sim N^{-1/2}$), the absolute cluster calibration would need to be better than 2.5%. For a fully targeted survey, about 14000 clusters, this cluster mass calibration uncertainty reduces to $> 1\%$.

2.5.2 Calibration of the Richness-Cluster Mass Relation

Large-scale optical surveys (e.g., DES and LSST) expect to detect hundreds of thousands of galaxy clusters at $z < 1$. Because they produce photometry only, a major challenge for these surveys is relating a cluster observable to the total DM mass. One promising cluster mass estimator is the optical richness (e.g., Abell 1958). Specifically, here, we use λ, the weighted number of galaxies within a scale aperture (e.g., Rozo et al. 2011) as calculated by the redMapper algorithm (Rykoff et al., 2012). Previous works (e.g., Rozo et al. 2010) show that the richness correlates strongly with cluster mass on the average, but the absolute mass scale of the optical richness mass estimator and the scatter in cluster mass at fixed optical richness are imprecisely known (Rykoff et al., 2012). These systematics remain the major source of uncertainty in deriving cosmological constraints from cluster abundances and must be measured using independent methods to realize the full potential of these types

of surveys.

The Buzzard cluster catalogs do not contain measurements of λ, so we supplement it by generating richnesses based on the true cluster masses. For testing we assume two versions of the richness-mass relationship. Farahi et al. (2016) base the relation on stacked velocity dispersions, and Simet et al. (2016) use weak lensing measurements to construct their relation. Because we are investigating HETDEX's ability to recover the underlying scatter in the mass-richness relationship, we use the true cluster masses perturbed by a known amount to estimate the observed richness.

As a check, after generating richness values we calculate the scatter of the masses at fixed λ, $\sigma_{M|\lambda}$ by comparing the true, unperturbed cluster masses against the richness and find that we do recover the expected scatter. We repeat the process with both assumed richness-mass relationships and recover the expected scatter in both instances.

Figure 2.8 summarizes the main results of this investigation. The top panel shows the generated optical richness, λ, versus the predicted cluster mass. The cluster masses are the $ML_{\sigma,z,N_{gal}}$ based and correspond to the targeted and survey observation strategies. The bottom panel of Figure 2.8 shows the scatter in the predicted cluster masses at fixed richness, $\sigma_{M|\lambda}$. The solid line represents the intrinsic amount of scatter added to the masses. The cluster masses are binned in increasing ten richness intervals ($10 - 20$, $20 - 30$, etc.). The inset upper panel shows the intrinsic scatter versus the recovered average scatter at fixed richness, $\langle \sigma_{M|\lambda} \rangle$ and illustrates how well the two observation strategies recover the intrinsic scatter.

We exclude clusters with $\lambda > 130$ both because there are very few of them which does not accurately reproduce a scatter and because the observational studies which we base our richnesses on do not include these clusters. We find that we are able to accurately recover an average intrinsic scatter of $0.2 < \langle \sigma_{M|\lambda} \rangle < 0.3$ dex, finding

41
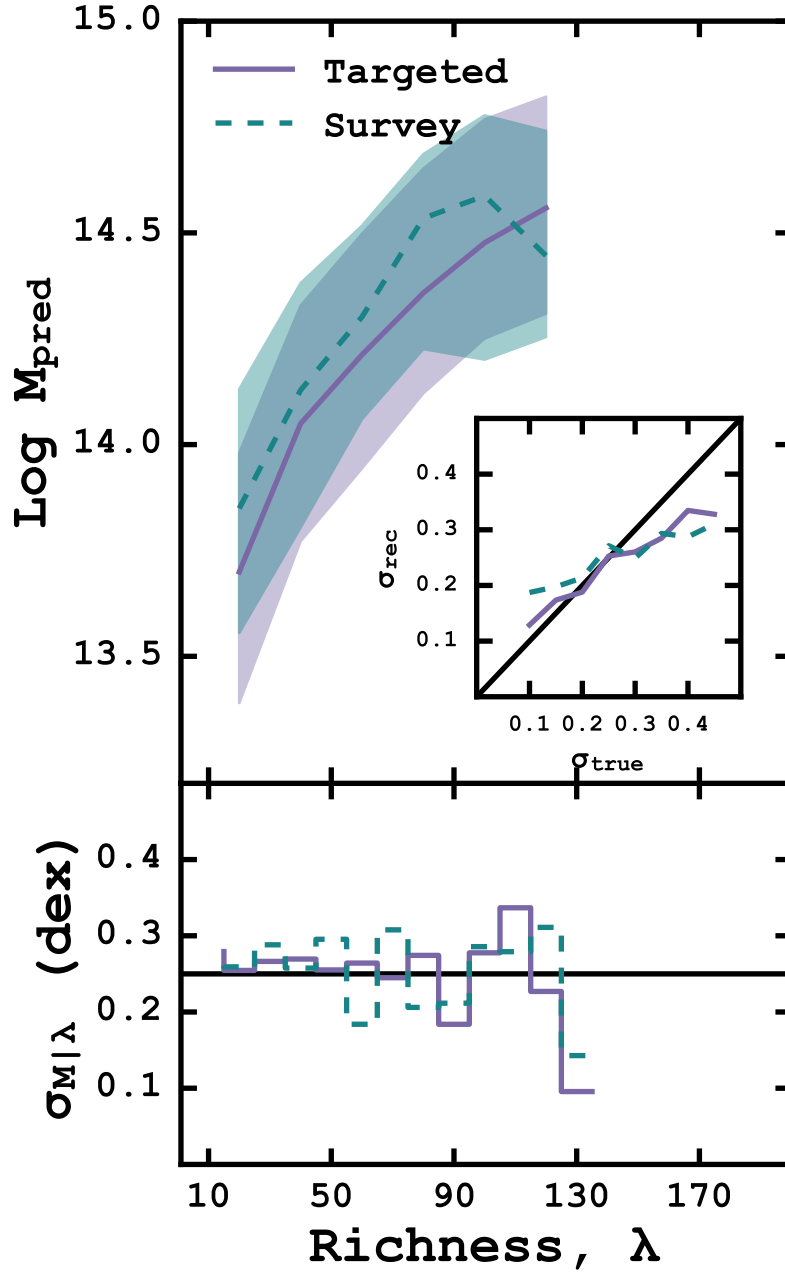
Figure 2.8: *Top*: The optical richness, λ, versus the predicted cluster mass. The solid, colored line is the median predicted mass for the targeted observing, and the colored, dashed line is the median recovered mass for the HETDEX-like observations. The shaded regions represent the 68% scatter around the median values. *Bottom*: The scatter in the relation at fixed richness. The solid black line shows the intrinsic scatter of $\sigma_{true} = 0.25$ dex. Color coding is the same as the top panel. *Inset*: The evolution of the intrinsic scatter versus the average recovered scatter, σ_{rec}. We find good agreement when intrinsic scatter is ~ 0.25 dex.

$\langle\sigma_{M|\lambda}\rangle = 0.255\pm0.02$ at $\sigma_{true} = 0.25$ with survey observations. This is very promising as other observational studies have estimated the intrinsic scatter of real clusters to be ~ 0.25 dex (e.g., Rozo & Rykoff 2014; Rozo et al. 2015a). As the intrinsic scatter increases or decreases, we fail to recover the scatter as accurately.

To get an idea of how well HETDEX will constrain the absolute mass scale we can find the best fitting relation to our richness-mass data. To generate the best fitting lines we follow the general procedure of Hogg et al. (2010), by defining an objective function and then minimizing the loss. Our objective function is

$$p(y_i|x_i, \sigma_{yi}, m, b, \sigma) = \frac{1}{\sqrt{2\pi\left(\sigma_{yi}^2 + \sigma^2\right)}} \exp\left(-\frac{[y_i - m\,x_i - b]^2}{2\left(\sigma_{yi}^2 + \sigma^2\right)}\right) \qquad (2.11)$$

where we consider both measurement errors in y_i, σ_{yi}, and intrinsic scatter, σ, in the relation between x_i and y_i. We assume that the intrinsic scatter is constant from point to point and that all of the measurement errors are Gaussian. We convert this objective function into a likelihood by multiplying all of the individual probabilities together,

$$\mathscr{L} = \prod_{i=1}^{N} p(y_i|x_i, \sigma_{yi}, m, b, \sigma). \qquad (2.12)$$

We again rely on MCMC samples to sample the posterior probability distribution and thus maximize the likelihood. The best fitting slope and intercept are quoted as the median value of the posterior probability distribution with 68% error bars defined as the 16th and 84th percentiles of the same distribution.

For a richness-mass relation with an intrinsic scatter of $\langle\sigma_{M|\lambda}\rangle = 0.25$, and following the more traditional parameterization of the richness-mass relation (e.g., Rykoff et al. 2012; Farahi et al. 2016), we find a best-fitting relation for the targeted obser-

vations as

$$\ln\left(\frac{M_{200c}}{h_{70}^{-1}10^{14}\mathrm{M}_\odot}\right) = 0.09 \pm 0.01 + 0.90 \pm 0.01 \ln\left(\frac{\lambda}{60}\right) \qquad (2.13)$$

and the survey observations as

$$\ln\left(\frac{M_{200c}}{h_{70}^{-1}10^{14}\mathrm{M}_\odot}\right) = 0.31 \pm 0.02 + 0.77 \pm 0.02 \ln\left(\frac{\lambda}{60}\right). \qquad (2.14)$$

This gives $M_{200c} = (1.09 \pm 0.01) \times 10^{14}h^{-1}$ $\mathrm{M}_\odot$and $M_{200c} = (1.36 \pm 0.03) \times 10^{14}h^{-1}$ $\mathrm{M}_\odot$ at $\lambda = 40$ for the targeted and survey observations respectively. If the intrinsic scatter is reduced to ~ 0.05 dex we recover an overall normalization of $M_{200c} = (1.6 \pm 0.02) \times 10^{14}h^{-1}$ $\mathrm{M}_\odot$ and $M_{200c} = (1.65 \pm 0.03) \times 10^{14}h^{-1}$ for the targeted and survey observations at $\lambda = 40$. In both cases, this normalization differs significantly from the $M_{200c} \approx 2.1 \times 10^{14}h^{-1}$ $\mathrm{M}_\odot$ found in recent work by Li et al. (2016); Simet et al. (2016).

2.6   SUMMARY

Here, we present detailed simulations of the upcoming HETDEX survey's applicability to the detection and total mass measurement of galaxy clusters. We use mock galaxy catalogs, and simulated, HETDEX-like observational strategies to estimate the number of clusters observed and the precision of their total mass estimates, using three different cluster mass estimators. We discuss HETDEX's ability to constrain the cosmological parameter $\sigma_8 h^{-1}$ and comment on how HETDEX may improve current and future photometric large-area sky surveys' cluster mass estimates derived from optical richness.

Our main conclusions are the following:

1. We find approximately 14000 clusters with at least five cluster members in the HETDEX cluster survey volume. Of those, approximately 1500 clusters

are detected with HETDEX-like survey observations. The number of cluster members recovered is almost exactly 4.5 times fewer than a fully targeted survey, across both a wide range of redshifts and cluster masses.

2. Overall, we find a traditional power-law conversion from LOSVD to cluster mass performs significantly poorer than either the probability based or ML based methods also tested. The probability based and ML based cluster mass estimators are able to more accurately predict cluster mass when combined with information other than just the LOSVD. While the power-law may be outperformed, overall, comparisons of similar mass galaxy clusters shows that above Log $M/M_\odot$ = 14.5, the power-law gives a lower bias than either the probability based or ML based methods. For HETDEX-like observations and clusters with $13 < \mathrm{Log}\, M/M_\odot < 14.5$, we find the $ML_{\sigma,z,N_{gal}}$ method performs the best. Below Log $M/M_\odot$ = 13 no method with survey observations gives an bias of less than 50%.

3. For followup targeted observations only galaxy clusters with masses inferred to be Log $M/M_\odot$ < 13 from survey observations should be targeted. Galaxy clusters with inferred masses below Log $M/M_\odot$ = 13 can see as much as an 81% improvement in cluster mass estimation with targeted observations. While the improvement of clusters with masses above Log $M/M_\odot$ = 13 is often approximately 10%.

4. For a cluster survey limited to $M > 10^{14}$ $M_\odot$ HETDEX's ability to constrain the cosmological parameter $\sigma_8 h^{-1}$ is at best $\sim 20\%$. This is significantly different than recent constraints from SZE surveys.

5. HETDEX will be able to place important constraints on the amount of scatter

in the optical richness-mass relationship. It will to a less extent constrain the overall normalization of the relation. This should provide an important too in the calibration of large-area sky surveys which rely on photometric data only to estimate cluster masses.

It is the author's hope that this work may be useful to others when conducting their own research. Because this work relies heavily on (often) complex data analysis, and in order to promote transparency and reproducible science, we provide all of the code used to conduct this study at https://github.com/boada/desCluster. Regrettably, large file size prevents including the source data with the analysis routines. The authors are happy to provide them, if requested.

3.   TARGETED OBSERVATIONS WITH THE VIRUS PROTOTYPE INSTRUMENT

3.1   INTRODUCTION

Clusters of galaxies form the largest bound objects in the universe, and as such their study is a cornerstone in modern day astronomy. Thought to form out of the primordial density fluctuations in the very early universe, the number and distribution of galaxy clusters across the sky is the finger print of the cosmology imprinted on the universe at its birth. The ΛCDM model of cosmology makes explicit predictions about the number and masses of galaxy clusters throughout the universe. Connecting these predictions to a set of, sufficiently large in size, observed clusters remains a principal problem. Specifically, the largest threat to modern, precision, cluster cosmology is not the identification of large numbers of clusters (the total number of clusters known is only going up) but the accurate recovery of galaxy cluster mass (e.g., Sehgal et al. 2011; Planck Collaboration 2013; Bocquet et al. 2015).

As mass is not a direct observable, a lot of work is underway to characterize galaxy cluster masses with an observable feature of galaxy clusters. Observed X-ray temperatures and luminosities correlate tightly with a cluster's dynamical mass (e.g., Mantz et al. 2010; Rykoff et al. 2014), especially for dynamically relaxed clusters (e.g., Mantz et al. 2015). The Sunyaev–Zel'dovich effect (SZE; Sunyaev & Zeldovich 1972), which uses the up–scattering of cosmic microwave background (CMB) photons to estimate cluster masses, provides accurate estimations of mass (e.g., Vanderlinde et al. 2010; Sehgal et al. 2011), but the ability to detect low mass galaxy clusters is currently limited by technology (e.g., Carlstrom et al. 2002). Optical studies (e.g., Rozo et al. 2010, 2015b) primarily use the richness (e.g., Abell 1958; Rykoff et al.

2012) or galaxy velocity dispersions to estimate the mass, and are often used to calibrate other mass estimators (e.g., Ruel et al. 2014; Sifón et al. 2015a).

Today, the greatest number of clusters are being discovered using large SZE surveys with the South Pole Telescope (SPT; Carlstrom et al. 2011) or the Atacama Cosmology Telescope (ACT; Swetz et al. 2011). However, deep, wide field optical surveys, such as the Dark Energy Survey (DES; The Dark Energy Survey Collaboration 2005) will discover many more, low mass clusters in the near future. Such clusters will rely on spectroscopic follow up to better constrain their dynamical mass. But, as the number of clusters grows to many tens of thousands, spectroscopic followup becomes unfeasible. Therefore, large, single telescope, spectroscopic surveys will be required to reduce systematics and calibrate the observable–mass relation to a level that will allow accurate mass estimations using other methods.

In this work, we present a pilot study of ten massive galaxy clusters using integral field spectroscopy with the Mitchell Spectrograph as a pilot program for the Hobby Eberly Dark Energy Experiment (HETDEX; Hill et al. 2008b) survey. HETDEX is a forthcoming blind spectroscopic survey that could potentially be used to accurately calibrate the observable–mass relation for a significant number of galaxy clusters at both extremes of the mass scale. At present, because HETDEX is designed to measure the dark energy equation of state at $z \sim 2$, the applicability to galaxy cluster science has not yet been investigated. We began this investigation with Boada (2016a) (hereafter Paper I). The second installment of this two part work, the goal of this study is to obtain spectroscopic redshifts of the individual cluster galaxies, determine the velocity dispersion and to infer each cluster's dynamical mass. This allows us to compare the inferred mass with other mass estimators (e.g., the clusters in this sample have deep *Chandra* or *XMM-Newton* X-ray data, and richness measurements) with the aim of reducing the scatter in the richness–mass relation,

$\sigma_{M|\lambda}$. The ability of HETDEX to further constrain optically derived masses is of paramount importance to upcoming large photometric surveys. This study provides insight into how well a HETDEX type survey will constrain mass estimations and cosmological parameters in the future.

The layout of this work is the following. In Section 3.2 we discuss the target selection and the setup of the MS used to conduct the observations. Section 3.3 describes the methods and tools used to reduce the observations. We present our redshift catalog, cluster members and cluster dynamical properties in Section 3.4. In Section 3.7, we compare and discuss the different mass estimations and remark on the applicability of these methods for HETDEX. Finally, we summarize this work in Section 3.8.

Throughout this paper, we use a concordance cosmological model ($\Omega_\Lambda = 0.7$, $\Omega_m = 0.3$, and $H_0 = 70$ km s^{-1}Mpc^{-1}), assume a Chabrier initial mass function (Chabrier, 2003), and use AB magnitudes (Oke, 1974) unless specifically noted.

3.2   DESIGN

3.2.1   Target Selection

We select clusters at $z = 0.2 - 0.3$ using two different methods and for two different purposes. Eight of the ten clusters are optically selected from Rykoff et al. (2012) using the *Sloan Digital Sky Survey* (SDSS; Blanton et al. 2001) Data Release 8. These clusters have high ($M_{DM} > 8 \times 10^{14}M_\odot$) optically traced mass (richness; discussed further below). The last two clusters are selected from the *XMM Cluster Survey* (XCS; Mehrtens et al. 2012) and correspond to individually measured X-ray temperatures of $T_X < 2.5$ keV. Such X-ray temperatures have inferred masses of 10^{14}M$_\odot > M_{DM} > 5 \times 10^{13}M_\odot$.

The optically selected clusters have many more members (see Table 3.3) than

Table 3.1: Galaxy clusters targeted with the MS: Cluster is our local name; z is the nominal (often photometric) redshift of the cluster.

Cluster	Alt. Name	RA (J2000)	DEC (J2000)	
c16p23+0p06	SOGRAS J0104+0003	01:04:55.369	+00:03:36.28	0.
c203p83+41p0	Abell 1763	13:35:20.092	+41:00:04.12	0.
c210p2+02p8	Abell 1835	14:01:01.965	+02:52:42.63	0.
c234p2+24p4	MaxBCG J234.23439+24.40877	15:36:56.253	+24:24:31.60	0.
c250p08+46p7	Abell 2219	16:40:19.812	+46:42:41.51	0.
c260p61+32p13	Abell 2261	17:22:27.182	+32:07:57.24	0.
c319p70+0p56	MaxBCG J319.70446+00.56035	21:18:49.069	+00:33:37.33	0.
c328p33+0p19	Abell 2392	21:54:22.936	+00:37:23.48	0.
XMMXCSJ124425.9+164758.0	WHL J124425.4+164756	12:44:25.203	+16:47:48.00	0.
XMMXCSJ125650.2+254803.2	...	12:56:49.999	+25:48:02.99	0.

the X-ray selected clusters which allows us to investigate the accuracy of our mass recovery methods at both cluster and group scales. See Table 3.1 for individual cluster sky positions and associated parameters.

3.2.2   The Mitchell Spectrograph

The Mitchell Spectrograph (MS; formerly known as VIRUS-P; Hill et al. 2008a) is an integral field unit (IFU) in a square array of 246 4.24″ diameter optical fibers. This provides a $1.7' \times 1.7'$ field-of-view (FOV) with a 1/3 filling factor. A Fairchild Instruments, 2k×2k charge couple device (CCD) images the spectra from each of the 246 fibers. The spectra have approximately a gaussian profile with a 5 pixel full width at half maximum (FWHM), and each are separated by 8 pixels to minimize the amount of cross-talk between the fibers.

There are two spectral configurations available on The Mitchell Spectrograph, a blue setup, 3600-5800 Å and a red setup, 4600-6800 Å. In addition, there are four volume phase holographic gratings available to disperse the light. For the purpose of this work, the lowest resolution, ~ 5Å, grating is used. Using 1×1 binning, this

translates into a spectral dispersion of ~ 1.11 Å pixel^{-1}.

3.2.3 Observations

We use the Mitchell Spectrograph to target the galaxy clusters using the 5Å grating covering a wavelength range of 4400 - 6600Å. With this instrumental setup and for galaxies $z = 0.2 - 0.3$, we will cover the Ca H&K, Fe I ($\lambda4383$), H-δ, H-γ and H-β absorption features. Additionally, we cover emission of the [O II] ($\lambda\lambda3727 - 3729$Å) doublet, H-$\beta$, and [O III] ($\lambda\lambda4960, 5008$), which allows for the identification of actively star-forming galaxies.

The FOV of the MS corresponds to an approximately 0.4 Mpc square region at $z = 0.2 - 0.3$. To ensure adequate coverage of the cluster out to 0.5 Mpc, we use four MS pointings per cluster. Figure 3.1 shows an example of the tiling done on each cluster. The northeast, northwest, southwest, and southeast fields with the fiber positions are shown in black, blue, green and purple respectively. The entire field is centered on the brightest cluster galaxy (BCG) and the individual tiles are shifted away. Furthermore, each of the four tiles are dithered at relative positions $(\Delta\alpha, \Delta\delta) = (0.0'', 0.0'')$, $(-3.6'', -2.0'')$, and $(0.0'', -4.0'')$ from the origin to ensure full coverage of the FOV. Therefore, there are 736 individual spectra for each of the four fields or 2952 measurements for the cluster as a whole.

Gotta talk to casey about these exposure times. I'm not sure how it all works out. We have set exposure times to achieve spectra with signal-to-noise ratios (SNRs) ~ 3 per spectral element in the continuum for objects with g = 21.3 mag (which corresponds to approximately 0.2L* for cluster galaxies at $z = 0.2$). We base the expected SNR on the experience of Shetrone et al. (2010), who achieves SNR = 100 per pixel in the continuum for point sources with B=16.5 mag at 4000Å in 4800 seconds. Therefore, for our faintest objects with B $\approx$ g = 21.3 mag, we expect to
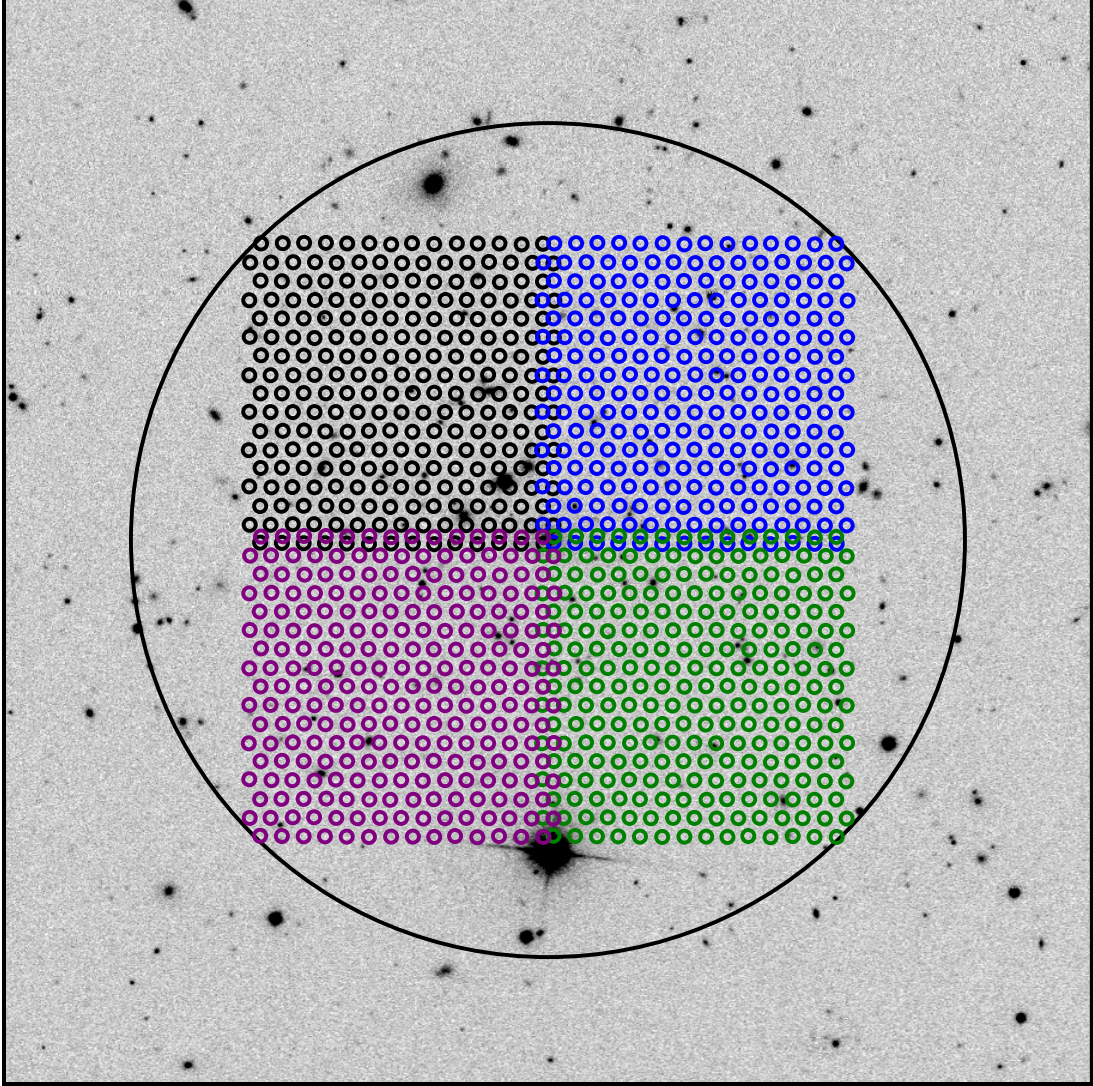
Figure 3.1: SDSS r-band image of an optically selected galaxy cluster selected from the SDSS DR8 data. The field is centered on the BCG, which has a measured spectroscopic redshift from SDSS of $z = 0.277$. The large black circle shows the region $R < 0.5$ Mpc ($r < 2.3'$). Nearly all galaxies within this region are associated with the cluster. The four MS fields (and fiber positions for the first dither position) are overdrawn on the field, illustrating how we survey each cluster.

achieve SNR = 3 per spectral element (averaged over 4.6 pixels) in 3600 seconds per pointing. We require 4 pointings to cover the full area for each cluster. Therefore, we require 1 hr/pointing × 4 pointings = 4 hrs on sky per cluster. Even though the field is dense with galaxies, there is sufficient "blank" area to allow for enough "sky" fibers for background subtraction. Therefore, no "sky" exposures are required. The math doesn't quite work out for the exposure times.

3.3   DATA REDUCTION

All data are reduced using P3D (Sandin et al., 2010) a general-use IFU reduction pipeline. The first step is to min/max-filtered average combine a minimum of twenty bias images from each night into a master-bias image, which is subtracted from each other image from the same night. Secondly, a trace mask is created from flat-fielding on the dusk or dawn sky. The fibers are fairly densely packed, so to determine the position of each spectrum in the dispersion direction each spectrum is extracted using a multi-profile deconvolution approach (Sharp & Birchall, 2010) to account for cross talk between fibers. Third, a dispersion mask for the wavelength calibration from images of Hg+Cd (for the May, 2012 observations) or Cd+Ne (for all other observations) arc lamps. The residuals between the derived wavelength solution and the known wavelengths of the emission lines is calculated from a fifth order polynomial and lie between. Finally, a fiber flat is created from the sky flats by a min/max-filtered average combine as in step one.

All that remains is the extraction of the science images, however there are several steps in this process. First, the science frames are bias subtracted. Next each frame is cleaned of cosmic ray hits using the PyCosmic (Husemann et al., 2012) integrated into P3D with the default parameters. Third the extracted spectra are wavelength calibrated using the previously created dispersion mask. Any flexure in

the instrument between the images of the arc lamps and science frames is accounted for by aligning the dispersion mask to bright telluric lines (namely 5577 Å). Finally the extracted spectra are normalized using the transmission in the fiber flat from above.

The result of this process is a row-stacked spectrum (RSS) where each of the 246 fibers are stored individually. A table of fiber positions maps each spectrum onto the image plane. However, for many of our observations a precise astrometric solution for the fiber positions is unknown. The position of the individual fibers but be recomputed by observing dense star fields after each telescope service in which the MS is involved. To correct our fiber positions we first identify fibers which observe stars and identify which fibers the astrometric solution indicates should contain stars. In many cases the stars are located between fibers. To account for this we use a simple Gaussian centroid weighted by the observed flux to find the correct sky position of the star. We then shift the fiber grid to match the sky position of the stars as reported by the SDSS. For each observation we use as many stars as possible and combine the shifts to generate a mean offset. This offset is applied to all dithers of each observation. There is little need to obtain highly accurate fiber positions as the 4.24″ fibers insures that reasonably correct positions will identify which fibers should and should not contain galaxies.

A simple sky subtraction scheme is used to remove the majority of sky contamination. Because the majority of fibers for any single pointing are empty, we use a 3σ clipped median selection to identify sky fibers and a simple average to combine them. The result is then subtracted from every fiber. This adequately removes the bulk of sky emission lines, but often fails to completely remove the

O I

line at 5577Å. This line is masked throughout the determination of redshifts.

After reducing all spectra we find an average residual mismatch in the wavelength solution of $\sigma_\lambda \sim 0.4$ Å or 24 km s^{-1}at 5000 Å. Fitting gaussians to each of the arc lines we find an average instrumental resolution of ~ 144 km s^{-1}, and combining the two in quadrature gives a total instrumental resolution of $\sigma_{inst} = 146$ km s^{-1}, similar to that of other studies using the MS (e.g., Murphy et al. 2011; Blanc et al. 2013).

3.4   ANALYSIS

The analysis of our reduced spectra occurs in two stages. First we derive individual redshifts using the observed galaxies, and then we work with the redshifts collectively to identify which galaxies likely belong to the galaxy cluster in question. This section outlines the steps required in each of those processes.

Individual galaxy selection is done through cross matching the IFU fiber sky positions with galaxies selected from the SDSS. We select all galaxies brighter than 22 mag in g within 3′ of the BCG in each cluster. For each galaxy we query the SDSS for photometry in all SDSS bands ($ugriz$), photometric redshift, and any spectroscopic redshift.

Because of the large number of fiber pointings, only fibers which overlap with SDSS sources are considered for redshift analysis. Figure **??** shows cluster c203p83+41p0 with the SDSS detections and measured redshifts overlaid. Orange diamonds are galaxies with SDSS available redshifts. The blue circles and red squares correspond to galaxies where a redshift was and was not determined from the observed spectra. See the appendix for similar figures of the remaining nine clusters.

3.4.1   Redshift Catalog

A redshift solution is determined for each galaxy by cross-correlating (Tonry & Davis, 1979) each of the spectra with six galaxy template spectra from the SDSS[1]

---

[1]http://classic.sdss.org/dr7/algorithms/spectemplates/index.html
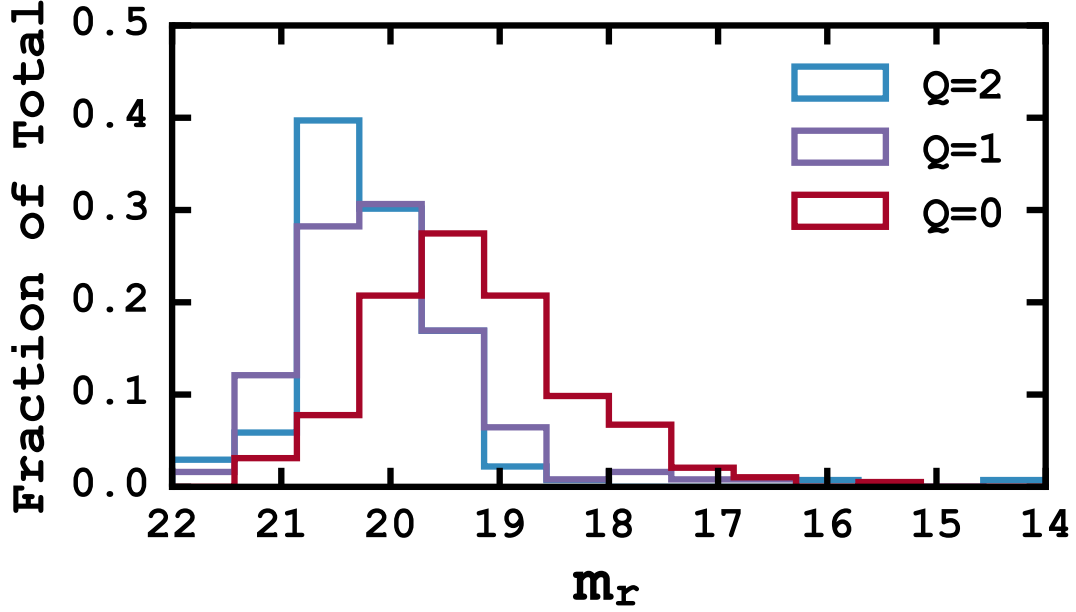
Figure 3.2: Redshift recovery fractions across all clusters. The bar heights represent the fraction of the total redshifts with the respective Q value at a particular magnitude. For example, $\sim 40\%$ of the $Q = 2$ redshifts have $m_r = 20.5 - 21$. We find a general decrease in redshift quality with increasing m_r.

using the XCSAO task in the IRAF RVSAO package (Kurtz et al., 1992; Kurtz & Mink, 1998). For each galaxy we select the spectral template with the highest cross-correlation coefficient and visually inspect the fit. During visual inspection a "Q" or quality flag is assigned. High-confidence redshifts, clearly determined by at least two obvious features (such as the Ca H, K and E absorption features), receive $Q = 0$, spectra with only a single strong feature (e.g., [

O II

] emission) are assigned $Q = 1$ and redshifts resulting from enigmatic features are assigned $Q = 2$. For the determination of cluster properties we only consider $Q = 0$ and $Q = 1$ quality flags.

Figure 3.2 shows the breakdown of Q values for the redshifts across all clusters. We compute 447 redshifts, of which 44% have $Q = 0$, 27% have $Q = 1$ and 29% have $Q = 2$. We find a general decrease in Q flag with increasing m_r. Approximately 30% of the $Q = 0$ redshifts correspond to galaxies with $19 < m_r < 20$ whereas about 40% $Q = 2$ galaxies have $m_r = 20.5 - 21$.

XCSAO reports errors on the cross-correlation redshift. Quintana et al. (2000) show that the cross-correlation errors are smaller than than the statistical errors by a factor of two. The redshift errors reported are twice the uncertainty reported by RVSAO.

Redshift information, with $Q = 0$ or $Q = 1$ spectra, for each galaxy are given in Table 3.2. The right panel of Figure **??** shows selected spectra from cluster c203p83+41p0 with corresponding best fitting SDSS template. See the appendix for similar examples from the remaining nine clusters.

3.4.2 Cluster Membership

The determination of cluster membership begins with the calculation of the cluster central redshift. This serves as a zero-point from which all other galaxies will be compared. Therefore, the accurate determination of the cluster redshift (z_c) is crucial to the reliability of all following measurements. An incorrect cluster redshift introduces errors into the measured line of sight velocity (LOSV) and corresponding dispersion, which, in turn, contributes to errors associated with dynamical mass and radius.

In simple terms, the cluster redshift is the mean of the redshifts of all galaxies associated with the cluster. However, because the standard mean can be quite sensitive to outliers or otherwise contaminated data, we require a more resistant statistic, and turn to the biweight location estimator (Beers et al., 1990) which provides im-

Table 3.2: Spectroscopic redshifts for galaxies in C203p8+41p0 measured with the MS: m_r is the observed SDSS r magnitude. z is the derived redshift. Q is the redshift quality flag; see Section 3.4.1. Member? indicates whether the galaxy is a member of the cluster; see Section 3.4.2. See the appendix for similar tables for the remaining nine clusters.

tile	dither	fiber	ra	dec	r (mag)	redshift	Q	Member	R (Mpc)
NE	1	14	13:35:27.004	+41:01:36.20	20.47	0.2019±0.0003	1	...	0.40
NE	1	111	13:35:24.177	+41:00:54.16	20.10	0.1178±0.0001	1	...	0.15
NE	1	154	13:35:23.853	+41:00:33.19	19.28	0.2214±0.0002	0	...	0.18
NE	2	6	13:35:21.777	+41:01:34.15	20.38	0.1691±0.0002	1	...	0.27
NE	2	14	13:35:26.632	+41:01:33.06	20.95	0.0403±0.0003	0	...	0.09
NE	2	63	13:35:20.998	+41:01:08.49	17.90	0.2381±0.0001	0	✓	0.25
NE	3	22	13:35:22.879	+41:01:24.60	19.76	0.2386±0.0003	0	✓	0.33
NE	3	25	13:35:24.669	+41:01:26.21	19.54	0.1444±0.0001	0	...	0.25
NE	3	73	13:35:18.447	+41:01:00.60	19.63	0.0779±0.0001	0	...	0.09
NE	3	106	13:35:20.957	+41:00:50.19	18.83	0.2235±0.0002	0	✓	0.17
NE	3	147	13:35:19.341	+41:00:31.82	19.48	0.2380±0.0001	0	...	0.11
NE	3	185	13:35:24.990	+41:00:18.06	20.51	0.1887±0.0002	1	...	0.18
NE	3	206	13:35:20.095	+41:00:04.12	16.39	0.2274±0.0001	1	✓	0.00
NE	3	210	13:35:22.528	+41:00:05.00	19.59	0.2242±0.0001	1	✓	0.10
NW	1	127	13:35:16.384	+41:00:47.33	17.43	0.2377±0.0001	0	✓	0.23
NW	1	167	13:35:14.400	+41:00:29.73	19.69	0.2333±0.0002	0	✓	0.26
NW	2	27	13:35:17.216	+41:01:27.25	20.21	0.1512±0.0002	0	...	0.24
NW	2	63	13:35:12.486	+41:01:10.57	18.84	0.1638±0.0001	0	...	0.31
NW	2	73	13:35:09.729	+41:01:03.49	20.00	0.2402±0.0001	1	...	0.50
NW	2	165	13:35:12.728	+41:00:25.16	18.74	0.2394±0.0001	0	✓	0.33
NW	2	171	13:35:16.434	+41:00:25.31	21.68	0.1617±0.0002	1	...	0.13
NW	2	173	13:35:17.911	+41:00:27.16	19.49	0.1039±0.0002	0	...	0.06
NW	2	220	13:35:10.891	+41:00:03.07	19.45	0.2994±0.0002	0	...	0.47
NW	2	239	13:35:13.582	+40:59:54.58	20.24	0.2316±0.0002	1	✓	0.28
NW	3	142	13:35:16.981	+41:00:35.55	19.44	0.2233±0.0002	0	✓	0.17
SE	1	27	13:35:25.896	+40:59:52.05	19.35	0.2295±0.0004	1	✓	0.25
SE	1	46	13:35:19.779	+40:59:41.85	18.73	0.2293±0.0002	0	✓	0.08
SE	1	86	13:35:26.506	+40:59:28.30	20.59	0.2255±0.0002	1	✓	0.29
SE	1	123	13:35:22.588	+40:59:11.02	18.17	0.2307±0.0002	0	✓	0.22
SE	1	129	13:35:26.254	+40:59:08.50	19.42	0.1282±0.0002	0	...	0.20
SE	2	164	13:35:20.600	+40:58:48.65	20.02	0.2938±0.0001	0	...	0.33
SE	3	157	13:35:25.857	+40:58:53.46	18.31	0.1701±0.0001	0	...	0.28
SE	3	171	13:35:25.332	+40:58:48.88	19.49	0.2400±0.0003	0	...	0.36
SE	3	198	13:35:24.191	+40:58:35.23	20.83	0.1177±0.0002	1	...	0.21
SW	1	41	13:35:17.295	+40:59:47.40	19.87	0.2231±0.0002	0	...	0.13
SW	1	114	13:35:17.529	+40:59:15.55	20.60	0.2493±0.0003	1	...	0.22
SW	1	224	13:35:13.709	+40:58:25.25	20.03	0.1276±0.0003	0	...	0.28
SW	1	227	13:35:15.509	+40:58:27.26	19.27	0.2328±0.0002	0	✓	0.41
SW	1	245	13:35:17.832	+40:58:19.02	19.29	0.2211±0.0003	1	...	0.39
SW	1	246	13:35:18.529	+40:58:20.43	21.31	0.1970±0.0002	1	...	0.34
SW	2	24	13:35:15.282	+40:59:51.52	21.29	0.2225±0.0002	1	✓	0.20
SW	2	29	13:35:18.391	+40:59:50.06	18.17	0.2405±0.0001	0	...	0.09

58

proved performance. The biweight location does not give us the freedom to use all galaxies measured but provides protection against a small number of interlopers. Therefore, the process of determining z_c and the cluster membership are linked. We begin with the nominal z_c (see Table 3.1) and apply and initial velocity cut of 5000 km s^{-1} to remove any foreground or background galaxies. Then, using the membership determination techniques described below we determine the member galaxies from which a new z_c is calculated. The entire process is repeated until convergence, usually within a single iteration. The cluster central redshift and associated 95% uncertainties, derived from bootstrap shuffling, are given in Table 3.3.

To reject the galaxies not associated with the targeted cluster, we employ two methods. For clusters with 20 or more $Q = 0$ or $Q = 1$ redshifts we use the "shifting gapped" method of Fadda et al. (1996), which combines both the positional and velocity information. Galaxies are first sorted by their radial separation from the cluster center (See 3.1) and binned into radial bins of at least 10 members. Once in the radial bins, the galaxies are sorted by the LOSV,

$$LOSV = c\frac{(z - z_c)}{(1 + z_c)} \tag{3.1}$$

where c is the speed of light in km s^{-1}, z is the redshift of the individual galaxy and z_c is the redshift of the cluster. Any galaxy with a LOSV greater than 1000 km s^{-1} of a neighboring galaxy (the velocity "gap") is rejected as an interloper. The procedure repeats until the number of galaxies stabilizes in the bin. Once the members have been identified we recompute z_c, LOSVs, and begin the membership selection again. This process is repeated until the number of member galaxies stabilizes.

For galaxy clusters with fewer than 20 $Q = 0$ or $Q = 1$ redshifts we employ the general method outlined in Wilman et al. (2005); Connelly et al. (2012) with small

changes. We assume an initial velocity dispersion, $\sigma(v)$, of $500(1 + z)$km s^{-1} and apply both redshift and spatial limits given by:

$$\delta(z)_{max} = 2\sigma(v)/c \tag{3.2}$$

and

$$\delta(r)_{max} = \frac{c \times \delta(z)_{max}}{bH(z)} \tag{3.3}$$

where $b = 9.5$ is the aspect ratio, $H(z) = H_0 E(z)$ and $E(z) = \sqrt{\Omega_m(1 + z^3) + \Omega_\Lambda}$. We select all galaxies with $|z - z_c| < \delta(z)_{max}$ and radial separation, R, $< \delta(r)_{max}$. During each step, we update both the z_c and $\sigma(v)$ using the identified members and this process is repeated until the number of member galaxies converges. To calculate the velocity dispersion we use the gapper estimator (discussed in detail in Section 3.4.3) which is corrected by 1.135 to account for the 2σ redshift space cut applied during membership determination.

Membership information for the galaxies observed around cluster c203p83+41p0 is given in the Member? column of Table 3.2. See the appendix for the membership of the other observed clusters.

3.4.3 Line-of-Sight Velocity Dispersion

To compute the line-of-sight velocity dispersion (LOSVD) of each cluster we follow the maximum likelihood method of Walker et al. (2006). We assume that the each galaxy is drawn from a Gaussian distribution centered on the mean cluster velocity and we maximize the log of the product of each cluster member's individual Gaussian probabilities (their Eq. 8):

$$\ln(p) = -\frac{1}{2}\sum_{i=1}^{N}\ln(\sigma_i^2 + \sigma_p^2) - \frac{1}{2}\sum_{i=1}^{N}\frac{(v_i - \langle u \rangle)^2}{(\sigma_i^2 + \sigma_p^2)} - \frac{N}{2}\ln(2\pi). \tag{3.4}$$

where σ_p, $\langle\mu\rangle$, and σ_i is the LOSVD, the average radial velocity and the error on the individual LOSVs respectively. To maximize the probability, we use EMCEE[2] (Foreman-Mackey et al., 2013), a Monte Carlo Markov Chain (MCMC) sampler, based on affine-invariant ensemble sampler (see Goodman & Weare 2010 for details on affine-invariant samplers). Using simple priors, $\langle\mu\rangle$ lies between the maximum and minimum LOSV and $0 < \sigma_p < 1400$ km s^{-1}, we draw twenty thousand samples from the posterior probability distribution. We report measured a LOSVD as the median value of the posterior probability distribution with 68% error bars defined as the 16th and 84th percentiles of the same distribution.

3.4.4 Dynamical Mass

This is currently an EXACT copy from the HETDEX paper. Recently, the relationship between the LOSVD and dynamical mass has been the focus of several studies (e.g., Evrard et al. 2008; Saro et al. 2013; Sifón et al. 2013; van der Burg et al. 2014), and a best fitting relationship for the mass enclosed by r_{200c} of the form

$$M_{200c} = \frac{10^{15}}{h(z)}\left(\frac{\sigma_{1D}}{A_{1D}}\right)^{1/\alpha} \mathrm{M}_\odot \tag{3.5}$$

with $A_{1D} = 1040\text{-}1140$ km s^{-1} (Munari et al. 2013; referred to as σ_{15} in Evrard et al. 2008 and other works), $\alpha = 1/3$, $h(z) = H(z)/100$, and σ_{1D} is the LOSVD of the velocity tracers (dark matter particles, subhalos or galaxies).

We adopt the scaling relation of Munari et al. (2013) with $A_{1D} = 1177 \pm 4.2$ km s^{-1} and $\alpha = 0.364 \pm 0.0021$ as the relation is calibrated through a cosmological simulation which uses galaxies (opposed to DM particles or subhalos) as the tracers of velocity. Kirk et al. (2015) find that this choice results in dynamical masses which are $16 - 26\%$ lower than masses obtained through the scaling relation of Evrard et al.

---

[2]http://dan.iel.fm/emcee/current/

(2008). This is due dynamical effects which act upon the galaxies but not the DM particles.

3.5   Machine Learning Methods

The goal of this section is to describe the methods used to create a suitable training set for a machine learning (ML) method to then predict the dynamical masses of the ten clusters in our sample. In order to accomplish this, we must first assign Q flags to a mock galaxy catalog which, as best possible, accurately reflect the actual observations described previously. This will allow us to construct a catalog which contains galaxies which closely resemble the observed galaxies.

We begin the discussion with a brief introduction to supervised ML methods and a discussion about the creation of the mock galaxy catalogs used in this analysis. We then discuss the process used to assign the Q flags and conclude with an overview of the method we use to make cluster mass predictions.

3.5.1   Supervised Machine Learning

ML is a subfield of computer science which provides tools to give computers the ability to infer the relationship between known variables without that relationship being explicitly programed. Supervised ML provides the algorithm with a set of known inputs, "features" in ML speak, and a set of desired outputs or "targets." The relationship between the features and targets is determined through the use of a training set. The ML algorithm is first provided with both the features and targeted which it uses to infer their relationship, then it is given a new set of features which it uses to predict the desired targets.

Because there are many different ML algorithms the initial training set is often broken into a train and test set. For both sets the desired targets are known, so they can be used to both train the ML method and to test how well it predicts the

desired targets. The performance achieved can be used to select the best ML method. Once an algorithm is selected we can attempt to optimize it by further splitting the training sample into a cross-validation (CV) set. We use 5-fold CV throughout.

Just as in Paper I, we rely on an ensemble ML method where we use many estimators and then combine them at the end to make the best possible prediction. The combination of estimators come in two flavors. Averaging methods average the final estimates together into a single prediction, and boosting estimators which seek to boost the predictive power by combining weak estimates at each step in the learning process.

A forest of randomized decision trees (or random forest; RF) is a type of ensemble method where the trees can be visualized as flow chart. The path through the flow chart (the trees) is decided by the values of the training features at each fork. RF use a random subset of the train data to decide which fork should be followed. The final prediction is the average of each tree's final value. We use RF methods implemented in the Scikit-Learn (Pedregosa et al., 2012) Python library.

3.5.1.1 The Buzzard Catalog

The "Buzzard" mock galaxy catalog (R. Wechsler et al., private communication) contains 238 million galaxies with r mag < 29 and $z \leq 8.7$. The galaxies are located in a 398.49 degree^2 portion of the sky and their luminosities are derived from a combination of Sub-halo Abundance Matching (ShAM; Reddick et al. 2013) and Adding Density Dependent Spectral Energy Distributions (ADDSED). The galaxies are assigned to the dark matter halos identified by the ROCKSTAR halo finder (Behroozi et al., 2013). See Paper I for a more thorough description of the process used to create the catalogs.

3.5.2 ML Based Observations

In order to create a mock dataset which resembles our actual observations we rely on the RF method as a classifier. The goal is to assign each galaxy in the Buzzard catalog a Q flag of either 0, 1 or 2 based on their observed magitudes in the five SDSS filters, $ugriz$, the ten combinations of possible colors, and the square of those colors. Acquaviva (2016) uses a similar feature set to predict the metallicity of SDSS galaxies with good effect.

The RF classifier is tasked with learning which combinations of magnitudes and colors best separates the three possible Q flags and to assign each Buzzard galaxy into one of those classes. The classifier is trained using the redshift catalog derived from our cluster observations (Section 3.4.1). The 447 observations are split into a training, CV and test sample. We use the training set to train the ML method, the CV set to tune the model parameters (often called hyper-parameters) and the test sample to verify how well our model classifies each galaxy. We also perform recursive feature elimination to remove features which contribute very little to the classification.

We compute two statistics to evaluate how well our model classifies the galaxies. The recall is the number predicted compared to the true number of classifications. The precision is the number of correct predictions compared to the total number of predictions for each class. In both cases the metrics range from zero to one, and higher numbers are better. For our optimized RF classifier we achieve overall recall and precision of $\sim 60\%$. For the individual classes (Q flags), the RF classifier performs significantly better when classifying $Q = 0$ and $Q = 2$ galaxies, with recall rates above 70%. The $Q = 1$ training galaxies have significant overlap between $Q = 0$ and $Q = 2$ (see Figure 3.2) which leads to a recall for $Q = 1$ galaxies of only $\sim 20\%$.
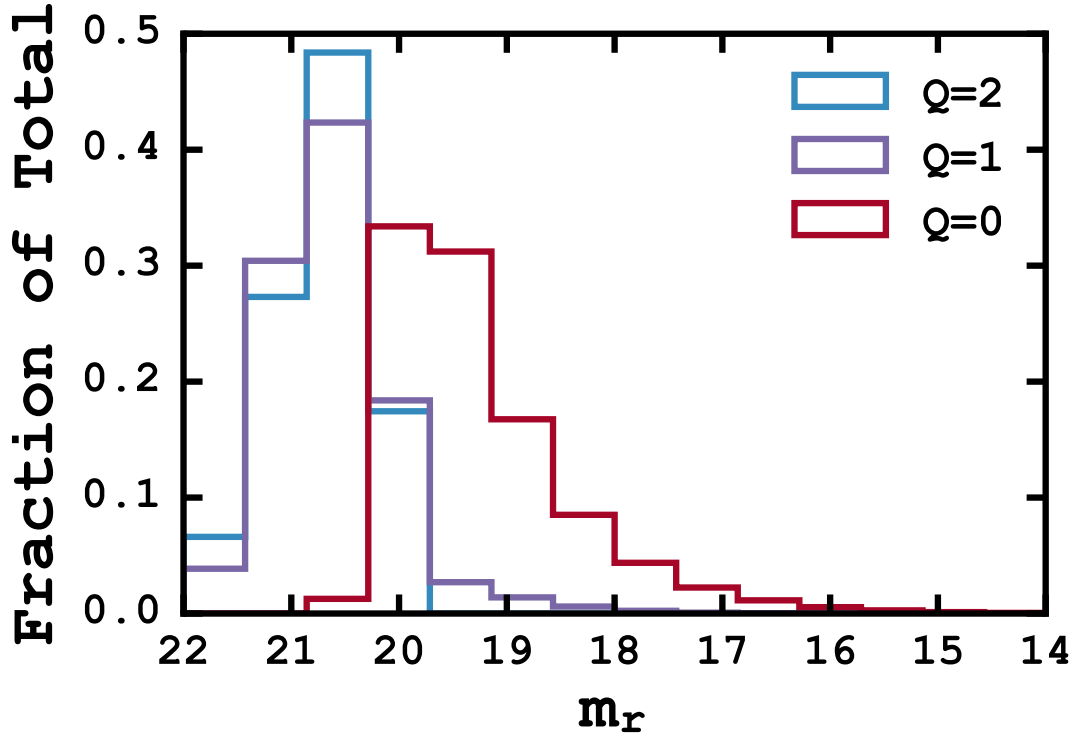
Figure 3.3: Quality flag (Q) assignments for the 2.7 million Buzzard catalog galaxies with $g < 22$ mag. The bar heights represent the fraction of the total redshifts with the respective Q value at a particular magnitude. The distributions resemble the actual observations in Figure 3.2. See the text for a detailed explanation of the classification process.

While not ideal, we find similar levels of recall for other ML classification methods.

We assign each galaxy in the Buzzard catalog with $z < 0.5$ and $g < 22$ mag a Q flag using the optimized RF classifier trained with all 447 observations. Figure 3.2 shows the Q flag distribution as a function of r magnitude. The total distribution of the 2.7 million Q flags is 45.6% $Q = 0$, 24.7% $Q = 1$, and 29.6% $Q = 2$. This distribution closely resembles the fractions of the actual observations with some $Q = 1$ galaxies misclassified as $Q = 0$. Because we use galaxies with either $Q = 0$ or $Q = 1$ this is not a large problem.

3.5.3   ML Based Cluster Masses

We use the "observed" galaxies created in the previous section to construct total mass distributions of the mock clusters. We use the method initially described in Paper I where we construct a ML estimator which predicts cluster mass when given a LOSVD, redshift and the number of galaxies observed. For this task we again use a RF, not as a classifier but as a regressor. Because the cluster masses presented with this method are predictions based on the feature data, any uncertainties quoted by this method are prediction intervals not confidence intervals. Prediction intervals are an estimate of the interval encompassing future observations, with a given probability. Confidence intervals, on the other hand, describe the different moments of a population. The prediction intervals are unique to each prediction, and are often based on the underlying assumption of normally distributed residuals. RF estimators do not assume normally distributed residuals, and thus, require special treatment.

The prediction intervals for our RF estimator as based on the method of quantile regression forests (Meinshausen, 2006). The basic principle is that we record all response variables (the predictions), not simply the mean. This allows us to given the prediction as the full conditional probability distribution of all possible predictions. For brevity, we quote predicted masses as the mean prediction and the 68% prediction interval as the 16th and 84th percentile of the full conditional probability distribution.

3.6   Results

In this section we present the derived properties of our ten clusters. We only consider galaxies which have a redshift quality flag of $Q = 0$ or $Q = 1$.
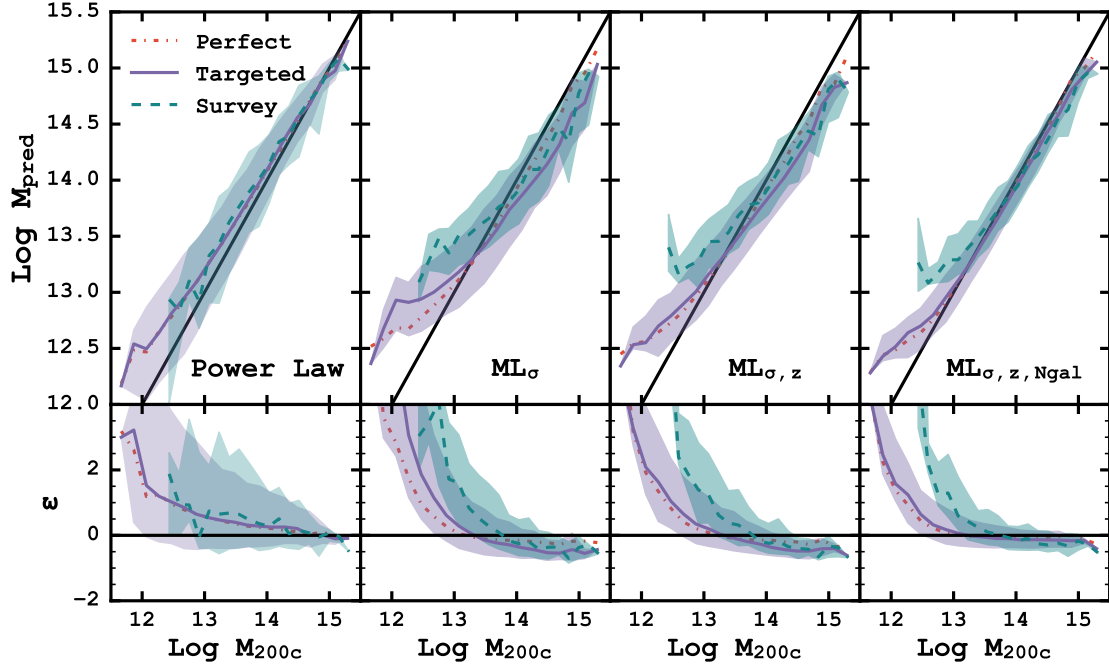
Figure 3.4: Mass predictions for the power law scaling relation (Equation 3.5) and the ML based technique with different input features as a function of true cluster mass. The bottom row of panels shows the fractional error (Equation 3.6) also as a function of true cluster mass. The solid black line shows the 1:1 relation. The solid, colored line is the median predicted mass for the targeted observing, and the colored, dashed line is the median recovered mass for the HETDEX-like observations. The shaded regions represent the 68% scatter around the median values.

3.6.1   Cluster Masses

In Paper I we found that the ML based method with the LOSVD (σ), redshift (z) and number of galaxies observed (N_{gal}) showed both the smallest bias and scatter over the largest range of cluster masses. Here we use the $ML_{\sigma,z,N_{gal}}$ method to estimate the masses of our ten clusters.

The prediction process uses two steps. Firstly, we use a method to predict the individual masses and secondly we correct those masses based on the results of the training data. The upper panel of Figure 3.4 show the cluster mass predictions for the Buzzard catalog clusters using the $ML_{\sigma,z,N_{gal}}$ method. We also include the standard power law scaling relation (Equation 3.5) for comparison. The black diagonal line shows the perfect 1:1 relation. The lower panel of Figure 3.4 show the fractional error

$$\epsilon = (M_{pred} - M_{200c})/M_{200c} \qquad (3.6)$$

as a function of true cluster mass.

Using the predicted cluster masses for the Buzzard catalog we can quantify the amount of bias, and the scatter about that bias for different bins of predicted cluster mass. The bias is correctable by simply shifting our predicted cluster mass up or down by the appropriate amount. The scatter estimates the overall mass scale uncertainty in each bin of predicted cluster mass. We report the uncertainties in our cluster mass estimates as the sum in quadrature of the prediction interval from the ML method and the mass scale uncertainty discussed here.

Table 3.3 presents a summary of the derived parameters for each cluster. We include the LOSVD, the estimated cluster redshift, and the number of member galaxies observed. We give two estimates of cluster mass, the uncorrected power-law based cluster mass and the corrected, $ML_{\sigma,z,N_{gal}}$ predicted mass. We take as a final pre-

Table 3.3: Summary of derived cluster parameters.

Cluster	Sources	Q=0 (1)	Members	z_c	σ (km s^{-1})	M_{200}
c16p23+0p06	0	10 (10)	15	0.2727±0.003	1187±145	12
c203p83+41p0	0	35 (17)	25	0.2310±0.002	1302±138	16
c210p27+2p87	0	14 (30)	16	0.2543±0.003	1302±91	16
c234p2+24p4	0	14 (14)	11	0.2255±0.003	923±186	6.
c250p08+46p7	0	36 (14)	32	0.2274±0.002	1168±121	12
c260p61+32p13	0	26 (18)	23	0.2260±0.002	1072±146	9.
c319p70+0p56	0	21 (8)	18	0.2750±0.003	806±152	4.
c328p33+0p19	0	19 (2)	16	0.2167±0.003	537±109	1.
XMMXCSJ124425.9+164758.0	0	11 (8)	6	0.2316±0.003	384±191	0.
XMMXCSJ125650.2+254803.2	0	8 (3)	3	0.2821±0.006	352±241	0.

diction the ML based cluster mass.

3.6.2   Richness-Mass

We found in Paper I that HETDEX will be able to accurately estimate the absolute calibration and intrinsic scatter of the optical-richness-cluster-mass relationship for a small range of intrinsic scatters. Here we use the ten clusters observed to do the same.

To find a best-fitting richness-mass relation for our data we are required to fit $y = mx + b$ considering measurement errors in richness and predicted cluster mass along with intrinsic scatter of the relation. We assume the intrinsic scatter is constant from point to point, and we assume (not necessarily correctly) that all measurement errors are Gaussian. With the assumption of all Gaussian scatters we have:

$$p(y_i|x_i) = \frac{1}{\sqrt{2\pi\sigma^2}} \exp\left(-\frac{[y_i - m x_i - b]^2}{2\sigma^2}\right) \tag{3.7}$$

69
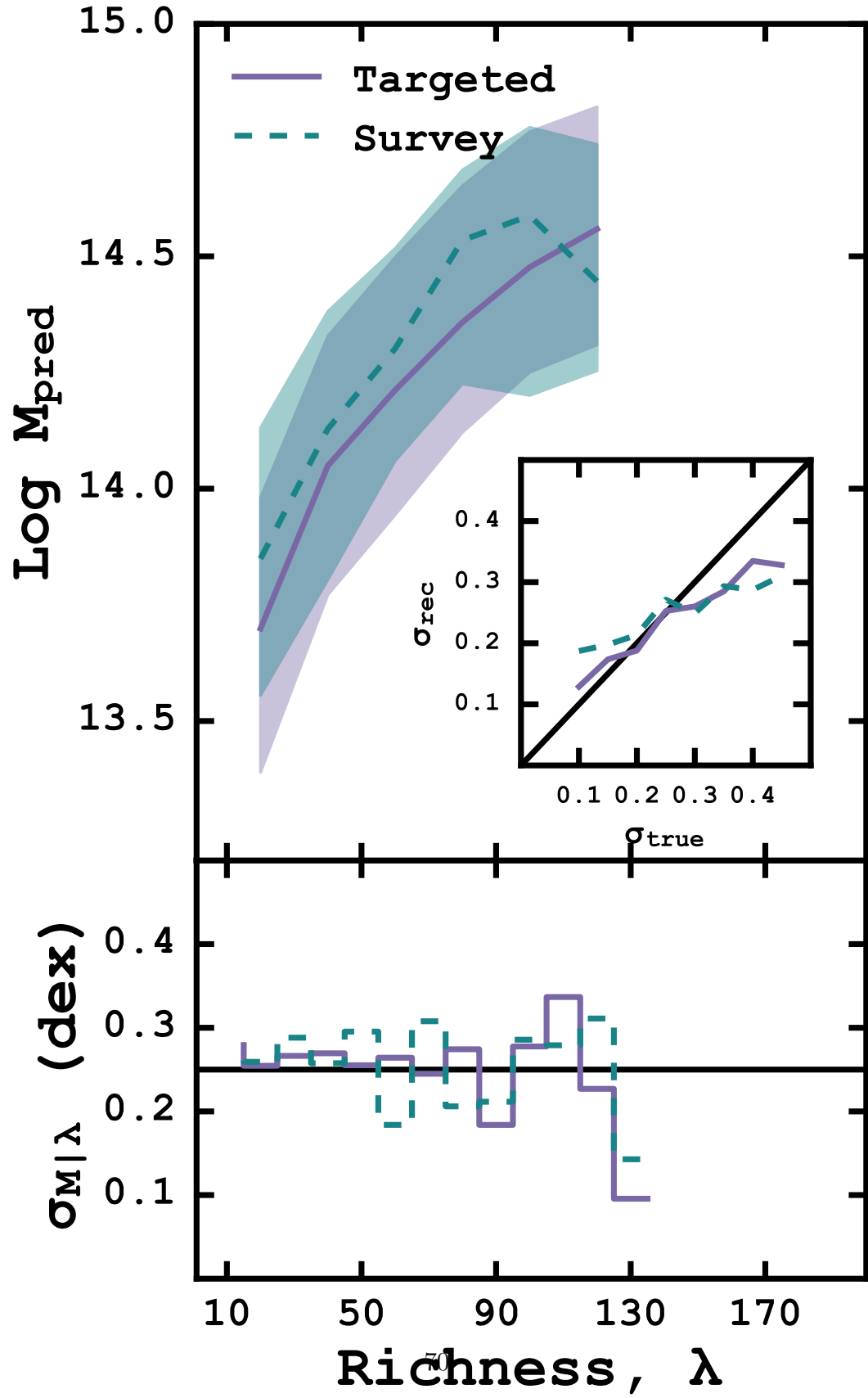
Figure 3.5: Richness, λ, versus total cluster mass for the clusters in our sample. The

for the intrinsic scatter,

$$p(\hat{x}_i|x_i) = \frac{1}{\sqrt{2\pi\sigma_{x,i}^2}} \exp\left(-\frac{[\hat{x}_i - x_i]^2}{2\sigma_{x,i}^2}\right) \tag{3.8}$$

and

$$p(\hat{y}_i|y_i) = \frac{1}{\sqrt{2\pi\sigma_{y,i}^2}} \exp\left(-\frac{[\hat{y}_i - y_i]^2}{2\sigma_{y,i}^2}\right) \tag{3.9}$$

for the measurement errors on the x and y variables respectively. We combine these three probabilities into

$$p(\hat{y}_i|\hat{x}_i) = \int_{-\infty}^{\infty} dy_i p(\hat{y}_i|y_i) \int_{-\infty}^{\infty} dx_i p(y_i|x_i) p(x_i|\hat{x}_i). \tag{3.10}$$

We assume flat priors on x_i so that $p(x_i|\hat{x}_i) = p(\hat{x}_i|x_i)$ and substitute our probability equations from above. We find that

$$p(\hat{y}_i|\hat{x}_i) =$$
$$\frac{1}{\sqrt{2\pi(\sigma^2 + \sigma_{y,i}^2 + m^2\sigma_{x,i}^2)}} \exp\left(-\frac{[y_i - m x_i - b]^2}{2(\sigma^2 + \sigma_{y,i}^2 + m^2\sigma_{x,i}^2)}\right) \tag{3.11}$$

which for $\sigma_{x,i}$ reduces to the familiar form of a Gaussian with a combination of measurement error and intrinsic scatter. We convert this probability function into a likelihood by multiplying all of the individual probabilities together,

$$\mathscr{L} = \prod_{i=1}^{N} p(\hat{y}_i|\hat{x}_i). \tag{3.12}$$

and maximize this likelihood by sampling from the posterior probability distribution. We quote the most probable slope and intercept as the median value of the posterior probability distributions with uncertainties as the 16th and 84th percentiles of the

same distribution.

We find a best fitting relation of

$$Log\,M = 1.17 \pm 0.39 \, \mathrm{Log}\, \lambda + 12.4863 \pm 0.82. \tag{3.13}$$

We convert this into a traditional parameterization of the richness-mass relation (e.g., Rykoff et al. 2012; Farahi et al. 2016) as the following, something needs to be done about the errors

$$\ln\left(\frac{M_{200c}}{h_{70}^{-1} 10^{14} \mathrm{M}_{\odot}}\right) = 0.47 + 1.17 \ln\left(\frac{\lambda}{30}\right). \tag{3.14}$$

We can estimate the intrinsic scatter in the relation two ways. Because our generative model includes an intrinsic scatter term, we can use the MCMC samples directly. We find $\sigma_{M|\lambda} = 0.22 \pm 0.13$ dex. We can also calculate the standard deviation of the residuals, which gives $\sigma_{M|\lambda} = 0.27 \pm 0.07$ dex. Both values fall into the range where HETDEX is most sensitive (Paper I), which is encouraging for the larger survey.

3.7 Discussion

3.7.1 Cluster Mass Accuracy

Unlike our simulated galaxies in the Buzzard catalogs, we do not know the true cluster mass for our ten observed clusters. Fortunately, seven of the ten have other measurements from the literature. Sifón et al. (2015a) report total cluster masses for four of our clusters. One has a reported LOSVD measurement and two have x-ray temperature measurements.

3.7.1.1   High Mass Clusters

Total mass estimates for our four highest mass clusters are also reported by Sifón et al. (2015a). Using spectra obtained with the Canada-France-Hawaii Telescope, they measure a LOSVD for each cluster. They convert the LOSVD into a dynamical cluster mass using the power law scaling relation of Evrard et al. (2008) (which is the basis of our Equation 3.5) and estimate the uncertainties using jackknife resampling.

Mass estimates for three of the four clusters overlap within the 1σ error estimates, but the fourth cluster, Abell 1835, differs by almost a decade. Abell 1835 is a relatively well studied cluster, providing several cluster mass estimates. Hoekstra et al. (2012) report a LOSVD for Abell 1835 of 1218^{+74}_{-70} km s^{-1}, compared to our 1302 ± 91 km s^{-1}. Geller et al. (2013) find $M_{200c} = (16.57 \pm 1.86) \times 10^{14}$ M$_\odot$ from the best fitting caustic mass profiles, which is similar to our reported value. Using *Chandra* X-ray observations, Bonamente et al. (2012) report a $M_{200c} = (8.35^{+0.81}_{-0.86}) \times 10^{14}$ M$_\odot$.

3.7.1.2   c328p33+0p19

The predicted mass of this cluster is significantly lower than expected. Previous work (Wing & Blanton, 2013) find it has a LOSVD of 1485 km s^{-1} significantly greater than our recovered value. It is not immediately clearly why we have recovered such a lower LOSVD. Wing & Blanton (2013) conducted a substructure study and found that c328p33+0p19 shows little to no signs of substructure. If we replace our LOSVD measurement and recompute the predicted cluster mass, we find $M_{200c} = 24.4 \times 10^{14}$ M$_\odot$.

3.7.1.3 XMMXCSJ124425.9+164758.0

With only six member galaxies identified, XMMXCSJ124425.9+164758.0 is near the very limit of our ability to produce accurate cluster mass estimates. Fortunately, the cluster has an measured x-ray temperature which we can use to as another estimate of mass. Its XCS data release 1^3 (Mehrtens et al., 2012) measured temperature is $1.3^{+0.2}_{-0.3}$ KeV which equates to $M_{500c} \approx 0.41 \times 10^{14}$ M$_\odot$ using the T_x-M relationship for low-temperature systems of Finoguenov et al. (2001).

We convert this predicted mass from M_{500c} to M_{200c} using the general prescription in Hu & Kravtsov (2003) to arrive at a predicted mass of $M_{200c} \approx 0.53 \times 10^{14}$ M$_\odot$, in reasonable agreement with our LOSVD predicted value of $M_{200c} \approx 0.59 \times 10^{14}$ M$_\odot$.

3.7.1.4 XMMXCSJ125650.2+254803.2

The three member galaxies identified in XMMXCSJ125650.2+254803.2 do not place a statistically strong constraint on the LOSVD predicted cluster mass. It too has a X-ray temperature measurement as part of XCS. Using the same approach as with XMMXCSJ124425.9+164758.0, a measured X-ray temperature of $1.4^{+0.2}_{-0.3}$ KeV gives a predicted cluster mass of $M_{200c} \approx 0.61 \times 10^{14}$ M$_\odot$. This is about 26% higher than our LOSVD derived cluster masses.

3.7.2 Calibration of the Richness-Mass Relation

Here we compare our fit of the richness-mass relation to a variety of constraints from the literature. Because we have selected our clusters from the redMapper catalog, we begin with the richness-mass relation from Rykoff et al. (2012). The authors suggest a power-law index of $\alpha = 1.08$ and an absolute mass scale of $M = (3.9 \pm 1.2) \times 10^{14}\, h^{-1}$ M$_\odot$ at $\lambda = 60$. we find ....

---

[3] http://www.astro.ljmu.ac.uk/ xcs/DR1/XCSDataRelease.html

With very careful handling of uncertainties, Simet et al. (2016) find the a normalization of Log $M/M_\odot = 14.344 \pm 0.021$(statistical)$\pm 0.023$(systematic) at $\lambda = 40$ with a power-law index of $\alpha = 1.33$.

Farahi et al. (2016) has also calibrated the richness-mass relation of redMapper clusters through stacked LOSVD measurements. They report a power-law index of $\alpha = 1.31 \pm 0.14$ and an absolute mass scale of $M_{200c} = (1.56 \pm 0.35) \times 10^{14}$ $M_\odot$, at $\lambda = 30$ and assuming $h = 0.7$.

The scatter around the richness-mass relation for the redMapper clusters has been estimated to be $\sigma_{M|\lambda} \sim 0.2 - 0.3$ dex (Rozo & Rykoff, 2014; Rozo et al., 2015a). This corresponds well to our estimate of $\sigma_{M|\lambda} \sim 0.25$ dex and the range most sensitively probed in our simulated HETDEX survey (Paper I).

3.8   SUMMARY

We carry out a proof-of-concept study where we present observations with the IFU Mitchelle Spectrograph of ten intermediate redshift ($z = 0.2 - 0.3$) galaxy clusters. We present an analysis where we use techniques to determine cluster membership and then predict cluster masses with a machine learning based pipeline. The goal of this study is to investigate how well a survey like HETDEX will be able to predict cluster masses and then use those masses to constrain the absolute calibration and intrinsic scatter in the optical richness-mass relation.

Our main results are as follows:

- We find our galaxy clusters have masses $(0.45 - 16.88) \times 10^{14}$ $M_\odot$. The majority of these estimates are consistent with other published values using a variety of estimation techniques.

- Using these cluster masses we fit a power-law to all ten clusters which gives a

best-fitting richness-mass relationship of:

$$\ln\left(\frac{M_{200c}}{h_{70}^{-1}10^{14}\mathrm{M}_\odot}\right) = 0.47 + 1.17\ln\left(\frac{\lambda}{30}\right). \tag{3.15}$$

with an overall normalization of $M_{200c} = 2.29 \times 10^{14}$ $\mathrm{M}_\odot$ at $\lambda = 30$ and an intrinsic scatter $\sigma_{M|\lambda} \sim 0.25$. Both of these properties compare well to other recent richness-mass studies.

It is the author's hope that this work may be useful to others when conducting their own research. Because this work relies heavily on (often) complex data analysis, and in order to promote transparency and reproducible science, we provide all of the code used to conduct this study at https://github.com/boada/vpCluster. Regrettably, large file size prevents including the source data with the analysis routines. The authors are happy to provide them, if requested.

REFERENCES

Abell, G. O. 1958, ApJS, 3, 211

Acquaviva, V. 2016, MNRAS, 456, 1618

Acquaviva, V., Gawiser, E., Leung, A. S., & Martin, M. R. 2014, Proc. IAU, 10, 365

Alam, S., Albareti, F. D., Prieto, C. A., et al. 2015, ApJS, 219, 12

Allen, S. W., Evrard, A. E., & Mantz, A. B. 2011, Annu. Rev. Astron. Astrophys., 49, 409

Annis, J., Soares-Santos, M., Strauss, M. A., et al. 2014, ApJ, 794, 120

Baxter, E. J., Rozo, E., Jain, B., Rykoff, E., & Wechsler, R. H. 2016, eprint arXiv:1604.00048, 7

Beers, T. C., Flynn, K., & Gebhardt, K. 1990, AJ, 100, 32

Behroozi, P. S., Wechsler, R. H., & Wu, H.-Y. 2013, ApJ, 762, 109

Blanc, G. a., Weinzirl, T., Song, M., et al. 2013, AJ, 145, 138

Blanton, M. R., Dalcanton, J., Eisenstein, D., et al. 2001, AJ, 121, 2358

Boada, S. 2016a, MNRAS

—. 2016b, MNRAS

Bocquet, S., Saro, A., Mohr, J. J., et al. 2015, ApJ, 799, 214

Bonamente, M., Landry, D., Maughan, B., et al. 2012, MNRAS, 428, 2812

Bond, J. R., Efstathiou, G., Lubin, P. M., & Meinhold, P. R. 1991, Phys. Rev. Lett., 66, 2179

Carlstrom, J. E., Holder, G. P., & Reese, E. D. 2002, Annu. Rev. Astron. Astrophys., 40, 643

Carlstrom, J. E., Ade, P. A. R., Aird, K. A., et al. 2011, PASP, 123, 568

Chabrier, G. 2003, PASP, 115, 763

Colless, M., Dalton, G., Maddox, S., et al. 2001, MNRAS, 328, 1039

Connelly, J. L., Wilman, D. J., Finoguenov, A., et al. 2012, ApJ, 756, 139

Crocce, M., Pueblas, S., & Scoccimarro, R. 2006, MNRAS, 373, 369

Croton, D. J., Springel, V., White, S. D. M., et al. 2006, MNRAS, 365, 11

de Haan, T., Benson, B. A., Bleem, L. E., et al. 2016, eprint arXiv:1603.06522, arXiv:1603.06522

De Lucia, G., & Blaizot, J. 2007, MNRAS, 375, 2

De Lucia, G., Springel, V., White, S. D. M., Croton, D., & Kauffmann, G. 2006, MNRAS, 366, 499

Eisenstein, D. J., Zehavi, I., Hogg, D. W., et al. 2005, ApJ, 633, 560

Evrard, A. E., Bialek, J., Busha, M., et al. 2008, ApJ, 672, 122

Fadda, D., Girardi, M., Iuricin, G., Mardirossian, F., & Mezzetti, M. 1996, ApJ, 473, 670

Farahi, A., Evrard, A. E., Rozo, E., Rykoff, E. S., & Wechsler, R. H. 2016, eprint arXiv:1601.05773, arXiv:1601.05773

Finoguenov, A., Reiprich, T. H., & Böhringer, H. 2001, Astron. Astrophys., 368, 749

Foreman-Mackey, D., Hogg, D. W., Lang, D., & Goodman, J. 2013, PASP, 125, 306

Geller, M. J., Diaferio, A., Rines, K. J., & Serra, A. L. 2013, ApJ, 764, 58

Goodman, J., & Weare, J. 2010, Commun. Appl. Math. Comput. Sci., 5, 65

Gott, J. R. I., & Rees, M. J. 1975, A&A, 45, 365

Hill, G. J., MacQueen, P. J., Smith, M. P., et al. 2008a, in Ground-based Airborne Instrum. Astron. II. Ed. by McLean, ed. I. S. McLean & M. M. Casali, Vol. 7014, 701470–701470–15

Hill, G. J., Gebhardt, K., Komatsu, E., et al. 2008b, Panor. Views Galaxy Form. Evol. ASP Conf. Ser., 399

Hill, G. J., Tuttle, S. E., Lee, H., et al. 2012, in Ground-based Airborne Instrum.

Astron. IV. Proc. SPIE, ed. I. S. McLean, S. K. Ramsay, & H. Takami, Vol. 8446, 84460N

Hoekstra, H., Mahdavi, A., Babul, A., & Bildfell, C. 2012, MNRAS, 427, 1298

Hogg, D. W., Bovy, J., & Lang, D. 2010, eprint arXiv:1008.4686, arXiv:1008.4686

Hu, W., & Kravtsov, A. V. 2003, ApJ, 584, 702

Hubble, E., & Humason, M. L. 1931, ApJ, 74, 43

Hubble, E. P. 1926, ApJ, 64, 321

Husemann, B., Kamann, S., Sandin, C., et al. 2012, A&A, 545, A137

Kelz, A., Jahn, T., Haynes, D., et al. 2014, in Proc. SPIE, ed. S. K. Ramsay, I. S. McLean, & H. Takami, Vol. 9147, 914775

Kirk, B., Hilton, M., Cress, C., et al. 2015, MNRAS, 449, 4010

Kravtsov, A. V., & Borgani, S. 2012, Annu. Rev. Astron. Astrophys., 50, 353

Kurtz, M. J., & Mink, D. J. 1998, PASP, 110, 934

Kurtz, M. J., Mink, D. J., Wyatt, W. F., et al. 1992, Astron. Data Anal. Softw. Syst. I, 25

Lemson, G., & The Virgo Consortium. 2006, eprint arXiv:astro-ph/0608019, arXiv:0608019

Li, R., Shan, H., Kneib, J.-P., et al. 2016, MNRAS, 458, 2573

LSST Dark Energy Science Collaboration. 2012, arXiv Prepr. arXiv1211.0310, 133

Mantz, A., Allen, S. W., Rapetti, D., & Ebeling, H. 2010, MNRAS, 406, no

Mantz, A. B., Allen, S. W., Morris, R. G., et al. 2015, MNRAS, 449, 199

Mehrtens, N., Romer, A. K., Hilton, M., et al. 2012, MNRAS, 423, 1024

Meinshausen, N. 2006, J. Mach. Learn. Res., 7, 983

Milvang-Jensen, B., Noll, S., Halliday, C., et al. 2008, A&A, 482, 419

Munari, E., Biviano, A., Borgani, S., Murante, G., & Fabjan, D. 2013, MNRAS, 430, 2638

Murphy, J. D., Gebhardt, K., & Adams, J. J. 2011, ApJ, 729, 129

Murray, S., Power, C., & Robotham, A. 2013, Astron. Comput., 3-4, 23

Neal, R. M. 1997, Markov Chain Monte Carlo Methods Based on 'Slicing' the Density Function, Tech. Rep. 9722, Department of Statistics, University of Toronto, Toronto, doi:10.1.1.48.886

Ntampaka, M., Trac, H., Sutherland, D. J., et al. 2015, eprint arXiv:1509.05409, arXiv:1509.05409

Oke, J. B. 1974, ApJS, 27, 21

Papovich, C., Shipley, H. V., Mehrtens, N., et al. 2016, eprint arXiv:1603.05660, 17

Pedregosa, F., Varoquaux, G., Gramfort, A., et al. 2012, J. Mach. Learn. Res., 12, 2825

Planck Collaboration. 2013, A&A, 571, 19

Press, W. H., & Schechter, P. 1974, ApJ, 187, 425

Quintana, H., Carrasco, E. R., & Reisenegger, A. 2000, AJ, 120, 511

Ramsey, L. W., Adams, M. T., Barnes III, T. G., et al. 1998, in Proc. SPIE, Vol. 3352, 34–42

Reddick, R. M., Wechsler, R. H., Tinker, J. L., & Behroozi, P. S. 2013, ApJ, 771, 30

Robotham, A. S. G., Norberg, P., Driver, S. P., et al. 2011, MNRAS, 416, 2640

Rozo, E., & Rykoff, E. S. 2014, ApJ, 783, 80

Rozo, E., Rykoff, E. S., Bartlett, J. G., & Melin, J.-B. 2015a, MNRAS, 450, 592

Rozo, E., Rykoff, E. S., Becker, M., Reddick, R. M., & Wechsler, R. H. 2015b, MNRAS, 453, 38

Rozo, E., Wu, H.-Y., & Schmidt, F. 2011, ApJ, 735, 118

Rozo, E., Wechsler, R. H., Rykoff, E. S., et al. 2010, ApJ, 708, 645

Ruel, J., Bazin, G., Bayliss, M., et al. 2014, ApJ, 792, 45

Rykoff, E. S., Koester, B. P., Rozo, E., et al. 2012, ApJ, 746, 178

Rykoff, E. S., Rozo, E., Busha, M. T., et al. 2014, ApJ, 785, 104

Sandin, C., Becker, T., Roth, M. M., et al. 2010, A&A, 515, A35

Saro, A., Mohr, J. J., Bazin, G., & Dolag, K. 2013, ApJ, 772, 47

Sehgal, N., Trac, H., Acquaviva, V., et al. 2011, ApJ, 732, 44

Sharp, R., & Birchall, M. N. 2010, Publ. Astron. Soc. Aust., 27, 91

Shetrone, M., Martell, S. L., Wilkerson, R., et al. 2010, AJ, 140, 1119

Sifón, C., Hoekstra, H., Cacciato, M., et al. 2015a, A&A, 575, A48

Sifón, C., Menanteau, F., Hasselfield, M., et al. 2013, ApJ, 772, 25

Sifón, C., Battaglia, N., Menanteau, F., et al. 2015b, eprint arXiv:1512.00910, arXiv:1512.00910

Simet, M., McClintock, T., Mandelbaum, R., et al. 2016, eprint arXiv:1603.06953, arXiv:1603.06953

Smith, S. 1936, ApJ, 83, 23

Spergel, D. N., Verde, L., Peiris, H. V., et al. 2003, ApJS, 148, 175

Springel, V. 2005, MNRAS, 364, 1105

Springel, V., White, S. D. M., Jenkins, A., et al. 2005, Nature, 435, 629

Sunyaev, R. A., & Zeldovich, Y. B. 1972, Comments Astrophys. Sp. Phys., 4

Swetz, D. S., Ade, P. A. R., Amiri, M., et al. 2011, ApJS, 194, 41

The Dark Energy Survey Collaboration. 2005, eprint arXiv:astro-ph/0510346, 42

Tinker, J., Kravtsov, A. V., Klypin, A., et al. 2008, ApJ, 688, 709

Tonry, J., & Davis, M. 1979, AJ, 84, 1511

Turner, E. L., & Gott, J. R., I. 1976, ApJS, 32, 409

van der Burg, R. F. J., Muzzin, A., Hoekstra, H., et al. 2014, A&A, 561, A79

Vanderlinde, K., Crawford, T. M., de Haan, T., et al. 2010, ApJ, 722, 1180

Walker, M. G., Mateo, M., Olszewski, E. W., et al. 2006, AJ, 131, 2114

Weinberg, D. H., Mortonson, M. J., Eisenstein, D. J., et al. 2013, Phys. Rep., 530,

White, S. D. M., & Rees, M. J. 1978, MNRAS, 183, 341

Wilman, D. J., Balogh, M. L., Bower, R. G., et al. 2005, MNRAS, 358, 71

Wing, J. D., & Blanton, E. L. 2013, ApJ, 767, 102

Zwicky, F. 1933, Helv. Phys. Acta, 6, 110

APPENDIX A

FIRST APPENDIX

Table A.1: Spectroscopic redshifts for galaxies in c16p23+0p06 measured with the MS: m_r is the observed SDSS r magnitude. z is the derived redshift. Q is the redshift quality flag; see Section 3.4.1. Member? indicates whether the galaxy is a member of the cluster; see Section 3.4.2. See the appendix for similar tables for the remaining nine clusters.

tile	dither	fiber	ra	dec	r (mag)	redshift	Q	Member	R (Mp
NE	1	223	01:04:56.937	+00:03:39.60	19.38	0.2691±0.0002	0	✓	0.10
NE	2	42	01:05:00.449	+00:04:57.41	19.80	0.2766±0.0001	1	✓	0.47
NE	2	168	01:04:58.247	+00:04:02.62	19.75	0.3054±0.0003	1	...	0.23
NE	2	216	01:05:00.487	+00:03:44.70	18.85	0.0826±0.0004	1	...	0.12
NE	2	220	01:04:55.367	+00:03:36.34	17.27	0.2715±0.0001	0	✓	0.00
NE	3	38	01:04:58.559	+00:04:55.13	19.95	0.3510±0.0001	1	...	0.46
NE	3	106	01:04:56.545	+00:04:23.15	18.36	0.2788±0.0001	0	✓	0.21
NE	3	118	01:04:55.276	+00:04:19.53	19.49	0.2747±0.0001	0	✓	0.18
NE	3	160	01:04:54.563	+00:04:00.66	18.19	0.2747±0.0001	0	✓	0.11
NW	1	156	01:04:53.064	+00:04:10.99	20.22	0.2234±0.0001	1	...	0.18
NW	2	173	01:04:54.217	+00:04:02.78	19.62	0.2629±0.0002	0	✓	0.13
NW	3	187	01:04:54.051	+00:03:52.42	19.35	0.3290±0.0001	1	...	0.12
SE	1	50	01:04:57.440	+00:03:17.71	19.51	0.2718±0.0002	1	✓	0.15
SE	2	191	01:04:55.332	+00:02:14.18	19.79	0.2794±0.0001	0	✓	0.35
SE	3	208	01:04:56.734	+00:02:05.07	18.75	0.2781±0.0001	0	✓	0.40
SE	3	238	01:04:57.284	+00:01:53.04	19.58	0.2705±0.0001	0	✓	0.45
SW	2	26	01:04:53.268	+00:03:26.04	18.99	0.2666±0.0002	0	✓	0.14
SW	2	135	01:04:49.814	+00:02:38.18	20.10	0.2697±0.0002	1	✓	0.42
SW	2	218	01:04:47.988	+00:01:59.05	19.55	0.2627±0.0001	1	✓	0.60
SW	3	228	01:04:52.934	+00:01:56.95	20.37	0.2763±0.0001	1	✓	0.45

Table A.2: Spectroscopic redshifts for galaxies in c234p2+24p4 measured with the MS: m_r is the observed SDSS r magnitude. z is the derived redshift. Q is the redshift quality flag; see Section 3.4.1. Member? indicates whether the galaxy is a member of the cluster; see Section 3.4.2. See the appendix for similar tables for the remaining nine clusters.

tile	dither	fiber	ra	dec	r (mag)	redshift	Q	Member	R (Mpc)
NE	1	78	15:36:58.192	+24:25:36.14	19.81	0.3228±0.0001	0	...	0.33
NE	1	124	15:36:59.468	+24:25:17.76	19.83	0.2324±0.0004	1	✓	0.24
NE	1	208	15:36:57.848	+24:24:41.47	20.35	0.1881±0.0001	0	...	0.08
NE	2	11	15:37:00.861	+24:26:04.40	20.48	0.0947±0.0001	1	...	0.20
NE	2	153	15:36:59.174	+24:25:04.55	20.37	0.1036±0.0002	1	...	0.10
NE	2	232	15:37:02.759	+24:24:34.63	19.98	0.3017±0.0001	1	...	0.40
NE	3	23	15:36:59.839	+24:25:59.51	18.05	0.1275±0.0000	0	...	0.23
NE	3	55	15:37:01.554	+24:25:45.67	19.79	0.2115±0.0001	1	...	0.36
NE	3	181	15:36:59.035	+24:24:48.56	20.11	0.1874±0.0001	1	...	0.13
NE	3	182	15:36:59.498	+24:24:50.78	19.62	0.1231±0.0003	1	...	0.11
NE	3	191	15:36:56.681	+24:24:43.40	19.54	0.1808±0.0000	0	...	0.04
NE	3	198	15:37:00.334	+24:24:44.60	17.27	0.2274±0.0002	0	✓	0.21
NE	3	210	15:36:58.911	+24:24:37.07	19.67	0.4813±0.0000	1	...	0.22
NE	3	219	15:36:56.253	+24:24:31.59	17.36	0.2262±0.0001	0	✓	0.00
NW	1	116	15:36:55.756	+24:25:25.38	18.90	0.2706±0.0001	1	...	0.23
NW	1	148	15:36:49.817	+24:25:04.96	20.02	0.2224±0.0001	0	✓	0.34
NW	2	26	15:36:54.106	+24:25:59.10	20.79	0.2298±0.0000	0	✓	0.34
NW	3	44	15:36:48.628	+24:25:45.78	21.29	0.3341±0.0001	1	...	0.62
NW	3	210	15:36:52.024	+24:24:36.09	19.78	0.2281±0.0001	0	✓	0.21
SE	1	48	15:36:57.612	+24:24:12.18	19.43	0.2215±0.0002	0	✓	0.10
SE	1	64	15:36:58.605	+24:24:04.80	20.06	0.2124±0.0001	1	...	0.15
SE	2	80	15:36:59.058	+24:23:57.63	19.24	0.2280±0.0002	0	✓	0.19
SE	2	95	15:36:59.393	+24:23:51.85	19.35	0.1244±0.0002	1	...	0.13
SE	3	108	15:36:58.708	+24:23:45.47	17.70	0.2235±0.0002	0	✓	0.21
SW	1	66	15:36:52.487	+24:24:08.35	20.29	0.1248±0.0001	1	...	0.13
SW	1	142	15:36:54.270	+24:23:37.37	20.15	0.2546±0.0001	0	...	0.24
SW	2	185	15:36:53.657	+24:23:15.33	19.58	0.2239±0.0002	0	✓	0.30
SW	3	65	15:36:51.996	+24:24:02.62	20.31	0.2201±0.0001	1	✓	0.23

Table A.3: Spectroscopic redshifts for galaxies in c250p08+46p7 measured with the MS: m_r is the observed SDSS r magnitude. z is the derived redshift. Q is the redshift quality flag; see Section 3.4.1. Member? indicates whether the galaxy is a member of the cluster; see Section 3.4.2. See the appendix for similar tables for the remaining nine clusters.

tile	dither	fiber	ra	dec	r (mag)	redshift	Q	Member	R (Mp
NE	1	34	16:40:21.617	+46:43:25.07	20.12	0.1014±0.0003	0	...	0.09
NE	1	110	16:40:23.879	+46:42:52.76	17.81	0.2333±0.0000	0	✓	0.16
NE	1	133	16:40:19.812	+46:42:41.30	16.61	0.2238±0.0001	0	✓	0.00
NE	1	156	16:40:25.818	+46:42:33.87	18.36	0.2099±0.0001	0	...	0.21
NE	1	183	16:40:24.352	+46:42:21.79	19.33	0.2248±0.0002	0	✓	0.18
NE	1	211	16:40:23.651	+46:42:10.01	17.62	0.2287±0.0001	0	✓	0.19
NE	2	65	16:40:22.597	+46:43:10.93	19.73	0.1813±0.0002	1	...	0.13
NE	2	81	16:40:23.696	+46:43:04.86	18.62	0.2324±0.0001	0	✓	0.17
NE	2	95	16:40:23.219	+46:42:58.04	19.32	0.2264±0.0001	0	✓	0.14
NE	2	122	16:40:22.018	+46:42:46.03	18.84	0.2079±0.0001	0	...	0.08
NE	2	136	16:40:21.428	+46:42:39.59	19.11	0.2180±0.0002	0	✓	0.06
NE	2	195	16:40:22.346	+46:42:14.63	19.21	0.2289±0.0002	0	✓	0.14
NE	3	37	16:40:23.777	+46:43:19.71	19.22	0.2229±0.0002	0	✓	0.20
NE	3	120	16:40:20.755	+46:42:43.96	17.82	0.2216±0.0002	0	✓	0.04
NE	3	181	16:40:23.067	+46:42:18.32	18.39	0.2191±0.0001	0	✓	0.14
NE	3	184	16:40:24.861	+46:42:18.39	19.09	0.2110±0.0002	0	...	0.20
NW	1	50	16:40:13.038	+46:43:18.14	19.37	0.2289±0.0002	0	✓	0.29
NW	1	79	16:40:13.042	+46:43:06.31	19.12	0.2297±0.0001	0	✓	0.27
NW	1	81	16:40:14.572	+46:43:04.50	20.49	0.2249±0.0002	1	✓	0.21
NW	1	128	16:40:16.854	+46:42:48.04	20.31	0.2281±0.0001	1	✓	0.11
NW	1	215	16:40:17.060	+46:42:11.27	19.21	0.2580±0.0002	1	...	0.17
NW	2	33	16:40:10.991	+46:43:22.18	19.33	0.2228±0.0001	1	✓	0.36
NW	2	56	16:40:16.794	+46:43:15.13	20.91	0.2350±0.0001	1	✓	0.17
NW	2	70	16:40:16.608	+46:43:09.56	20.70	0.2167±0.0002	1	✓	0.15
NW	2	81	16:40:14.180	+46:43:05.00	19.20	0.2252±0.0001	0	✓	0.23
NW	2	156	16:40:15.807	+46:42:31.47	18.88	0.2281±0.0002	0	✓	0.16
NW	3	33	16:40:11.463	+46:43:19.95	19.11	0.2249±0.0002	0	✓	0.34
NW	3	65	16:40:13.553	+46:43:08.81	20.49	0.1319±0.0001	1	...	0.16
NW	3	74	16:40:09.583	+46:43:03.29	20.34	0.1735±0.0001	1	...	0.32
NW	3	122	16:40:12.635	+46:42:44.68	19.66	0.2270±0.0001	0	✓	0.27
NW	3	144	16:40:18.116	+46:42:35.97	19.27	0.2080±0.0002	1	...	0.06
NW	3	149	16:40:11.390	+46:42:31.31	20.02	0.0844±0.0002	1	...	0.14
SE	1	4	16:40:20.674	+46:41:59.40	20.48	0.2341±0.0001	0	✓	0.16
SE	1	50	16:40:22.486	+46:41:42.33	20.51	0.2376±0.0002	1	...	0.25
SE	1	107	16:40:21.903	+46:41:15.96	18.82	0.1866±0.0001	0	...	0.28
SE	1	147	16:40:19.343	+46:40:57.31	18.39	0.1864±0.0001	0	...	0.33
SE	1	211	16:40:23.625	+46:40:32.22	19.06	0.2325±0.0001	0	✓	0.50
SE	1	214	16:40:25.819	+46:40:33.21	19.03	0.2272±0.0002	0	✓	0.52
SE	2	113	16:40:25.565	+46:41:14.28	20.51	0.2221±0.0002	0	✓	0.38
SE	2	165	16:40:21.553	+46:40:47.83	18.59	0.2110±0.0001	1	...	0.40
SE	3	18	16:40:20.484	+46:41:48.57	18.80	0.2347±0.0001	0	✓	0.20
SE	3	77	16:40:21.250	+46:41:25.01	18.21	0.1892±0.0001	0	...	0.25

Table A.4: Spectroscopic redshifts for galaxies in c210p27+2p87 measured with the MS: m_r is the observed SDSS r magnitude. z is the derived redshift. Q is the redshift quality flag; see Section 3.4.1. Member? indicates whether the galaxy is a member of the cluster; see Section 3.4.2. See the appendix for similar tables for the remaining nine clusters.

tile	dither	fiber	ra	dec	r (mag)	redshift	Q	Member	R (Mp
NE	1	6	14:01:04.022	+02:54:20.65	19.01	0.2478±0.0002	0	✓	0.40
NE	1	16	14:01:01.771	+02:54:13.80	20.37	0.3158±0.0002	1	...	0.42
NE	1	123	14:01:04.410	+02:53:29.95	19.70	0.2325±0.0002	1	...	0.22
NE	2	43	14:01:07.682	+02:54:03.80	20.20	0.2039±0.0001	1	...	0.40
NE	2	64	14:01:03.691	+02:53:52.63	20.48	0.2876±0.0002	1	...	0.32
NE	2	222	14:01:03.134	+02:52:45.00	18.66	0.2517±0.0002	0	✓	0.07
NE	3	63	14:01:03.475	+02:53:50.51	18.68	0.2598±0.0002	0	✓	0.29
NE	3	65	14:01:04.494	+02:53:50.70	20.31	0.2540±0.0002	0	✓	0.31
NE	3	79	14:01:04.203	+02:53:45.54	20.26	0.2192±0.0001	1	...	0.25
NE	3	114	14:01:07.185	+02:53:30.54	20.11	0.2606±0.0002	1	✓	0.37
NE	3	198	14:01:05.757	+02:52:54.15	19.70	0.2516±0.0002	0	✓	0.23
NE	3	237	14:01:03.483	+02:52:35.96	18.94	0.3110±0.0001	1	...	0.11
NW	1	23	14:00:58.786	+02:54:14.18	20.07	0.2318±0.0001	1	...	0.38
NW	1	92	14:00:57.098	+02:53:42.10	18.42	0.2108±0.0002	0	...	0.32
NW	1	105	14:00:56.404	+02:53:36.25	18.55	0.2504±0.0002	0	✓	0.39
NW	1	111	14:00:59.191	+02:53:33.62	19.78	0.2458±0.0002	0	✓	0.25
NW	2	103	14:00:55.146	+02:53:33.41	21.44	0.1642±0.0003	1	...	0.32
NW	2	119	14:00:55.968	+02:53:27.36	20.34	0.3084±0.0003	1	...	0.46
NW	2	127	14:00:59.815	+02:53:26.69	19.29	0.2723±0.0001	1	...	0.23
NW	3	13	14:01:00.752	+02:54:14.53	17.96	0.2492±0.0002	1	✓	0.37
NW	3	62	14:00:56.466	+02:53:49.12	20.53	0.3932±0.0001	1	...	0.57
NW	3	95	14:00:58.558	+02:53:38.37	20.03	0.2363±0.0001	1	...	0.28
NW	3	98	14:00:59.942	+02:53:37.00	20.63	0.4784±0.0000	1	...	0.37
NW	3	138	14:00:58.352	+02:53:20.29	18.69	0.2557±0.0002	0	✓	0.26
NW	3	168	14:00:58.824	+02:53:07.37	18.61	0.2321±0.0001	0	...	0.20
NW	3	211	14:00:58.625	+02:52:47.07	20.02	0.1463±0.0002	1	...	0.13
SE	1	90	14:01:02.616	+02:52:04.19	19.19	0.2639±0.0002	1	✓	0.16
SE	1	234	14:01:02.016	+02:51:03.83	21.20	0.2830±0.0002	1	...	0.42
SE	2	56	14:01:06.778	+02:52:19.68	17.90	0.2249±0.0002	1	...	0.27
SE	2	72	14:01:07.685	+02:52:16.24	20.08	0.3193±0.0002	0	...	0.42
SE	3	103	14:01:01.894	+02:51:52.53	19.80	0.2437±0.0001	1	✓	0.19
SE	3	127	14:01:06.471	+02:51:48.78	19.58	0.2726±0.0001	1	...	0.36
SW	1	57	14:01:01.072	+02:52:22.71	20.15	0.1615±0.0002	0	...	0.07
SW	1	144	14:01:01.183	+02:51:45.62	20.01	0.2670±0.0002	0	✓	0.24
SW	2	58	14:01:01.278	+02:52:21.62	20.96	0.2581±0.0001	1	✓	0.09
SW	2	65	14:00:57.802	+02:52:13.21	20.18	0.4127±0.0002	1	...	0.38
SW	2	98	14:00:59.802	+02:52:01.88	19.31	0.2549±0.0002	1	✓	0.21
SW	2	148	14:00:55.880	+02:51:36.29	21.24	0.1548±0.0002	1	...	0.30
SW	2	231	14:01:00.954	+02:51:06.98	20.55	0.3329±0.0001	1	...	0.46
SW	3	128	14:01:00.529	+02:51:49.71	18.25	0.2628±0.0003	1	✓	0.23
SW	3	169	14:00:59.240	+02:51:28.42	21.07	0.4035±0.0001	1	...	0.46
SW	3	187	14:01:00.832	+02:51:23.59	20.68	0.1628±0.0001	1	...	0.23

87

Table A.5: Spectroscopic redshifts for galaxies in c260p61+32p13 measured with the MS: m_r is the observed SDSS r magnitude. z is the derived redshift. Q is the redshift quality flag; see Section 3.4.1. Member? indicates whether the galaxy is a member of the cluster; see Section 3.4.2. See the appendix for similar tables for the remaining nine clusters.

tile	dither	fiber	ra	dec	r (mag)	redshift	Q	Member	R (Mp
NE	1	21	17:22:29.818	+32:09:29.21	20.20	0.1014±0.0004	0	...	0.18
NE	1	29	17:22:34.413	+32:09:25.72	19.68	0.2321±0.0001	0	✓	0.47
NE	2	32	17:22:27.631	+32:09:18.17	19.76	0.2200±0.0002	0	...	0.29
NE	2	62	17:22:28.177	+32:09:05.94	19.38	0.2246±0.0001	1	✓	0.25
NE	2	179	17:22:28.895	+32:08:16.78	19.86	0.2332±0.0002	1	✓	0.11
NE	3	42	17:22:33.506	+32:09:18.50	20.35	0.2318±0.0001	1	✓	0.42
NE	3	73	17:22:26.441	+32:08:58.70	19.12	0.2084±0.0001	0	...	0.21
NE	3	98	17:22:32.542	+32:08:52.14	20.50	0.2100±0.0003	1	...	0.30
NE	3	102	17:22:26.378	+32:08:45.31	19.76	0.1683±0.0001	0	...	0.14
NE	3	128	17:22:32.971	+32:08:38.74	19.34	0.2315±0.0001	1	...	0.31
NE	3	167	17:22:30.347	+32:08:20.40	19.86	0.2909±0.0002	1	...	0.20
NE	3	219	17:22:27.184	+32:07:57.25	15.38	0.2226±0.0002	0	✓	0.00
NW	1	102	17:22:18.160	+32:08:42.50	18.84	0.2228±0.0001	0	✓	0.44
NW	1	200	17:22:24.352	+32:08:04.74	20.42	0.2744±0.0001	1	...	0.15
NW	1	205	17:22:18.953	+32:07:57.82	19.67	0.2275±0.0001	0	✓	0.38
NW	2	68	17:22:23.220	+32:08:57.64	21.00	0.2798±0.0002	1	...	0.33
NW	2	116	17:22:25.574	+32:08:39.54	17.80	0.1685±0.0001	0	...	0.14
NW	2	148	17:22:19.197	+32:08:20.80	18.98	0.2245±0.0001	0	✓	0.38
NW	2	161	17:22:18.289	+32:08:12.33	19.59	0.2203±0.0002	0	✓	0.41
NW	2	163	17:22:19.559	+32:08:15.27	19.47	0.2143±0.0001	0	...	0.34
NW	3	26	17:22:24.290	+32:09:12.65	19.16	0.1680±0.0003	0	...	0.24
NW	3	50	17:22:21.475	+32:09:02.84	19.02	0.2260±0.0002	0	✓	0.36
NW	3	184	17:22:23.454	+32:08:06.50	19.96	0.2628±0.0001	1	...	0.20
NW	3	206	17:22:19.500	+32:07:52.06	20.94	0.2185±0.0001	1	✓	0.35
SE	1	202	17:22:33.893	+32:06:35.34	18.68	0.2203±0.0001	1	✓	0.42
SE	2	91	17:22:28.227	+32:07:18.12	20.29	0.2135±0.0001	0	...	0.14
SE	2	189	17:22:26.261	+32:06:33.18	20.64	0.2897±0.0002	1	...	0.37
SE	2	226	17:22:30.791	+32:06:22.27	20.60	0.2482±0.0001	1	...	0.41
SE	3	45	17:22:27.117	+32:07:35.51	19.77	0.2210±0.0003	0	✓	0.08
SE	3	171	17:22:32.779	+32:06:43.69	20.61	0.2261±0.0000	0	✓	0.37
SW	1	160	17:22:18.982	+32:06:49.70	19.60	0.2262±0.0001	0	✓	0.45
SW	1	203	17:22:26.919	+32:06:36.74	18.29	0.2256±0.0002	0	✓	0.29
SW	1	214	17:22:24.770	+32:06:30.20	20.93	0.2334±0.0001	1	✓	0.34
SW	2	121	17:22:21.021	+32:07:05.24	19.59	0.2293±0.0002	0	✓	0.35
SW	3	5	17:22:21.443	+32:07:53.68	19.98	0.1781±0.0002	0	...	0.22
SW	3	23	17:22:23.499	+32:07:47.19	19.62	0.1771±0.0001	0	...	0.14
SW	3	53	17:22:23.894	+32:07:32.82	20.45	0.3593±0.0001	1	...	0.24
SW	3	58	17:22:26.813	+32:07:34.55	19.46	0.2238±0.0001	0	✓	0.08
SW	3	89	17:22:19.677	+32:07:15.96	19.83	0.2258±0.0001	0	✓	0.38
SW	3	144	17:22:26.332	+32:06:55.93	20.24	0.2292±0.0001	1	✓	0.23
SW	3	146	17:22:19.254	+32:06:49.42	19.04	0.2258±0.0001	0	✓	0.44
SW	3	162	17:22:19.860	+32:06:44.09	19.95	0.3840±0.0001	1	...	0.62

Table A.6: Spectroscopic redshifts for galaxies in c319p70+0p56 measured with the MS: m_r is the observed SDSS r magnitude. z is the derived redshift. Q is the redshift quality flag; see Section 3.4.1. Member? indicates whether the galaxy is a member of the cluster; see Section 3.4.2. See the appendix for similar tables for the remaining nine clusters.

tile	dither	fiber	ra	dec	r (mag)	redshift	Q	Member	R (Mp
NE	1	193	21:18:50.285	+00:33:52.08	20.09	0.2785±0.0002	0	✓	0.10
NE	1	216	21:18:54.243	+00:33:45.76	19.71	0.2765±0.0001	0	✓	0.33
NE	2	220	21:18:49.071	+00:33:37.32	17.42	0.2756±0.0001	0	✓	0.00
NE	3	21	21:18:51.226	+00:35:01.96	19.56	0.2740±0.0002	1	✓	0.38
NE	3	66	21:18:51.814	+00:34:44.38	20.20	0.3058±0.0004	1	...	0.36
NE	3	75	21:18:49.304	+00:34:36.62	19.15	0.1346±0.0001	0	...	0.14
NE	3	77	21:18:50.210	+00:34:37.07	20.14	0.2195±0.0003	1	...	0.22
NE	3	118	21:18:49.121	+00:34:20.26	18.85	0.2610±0.0003	1	...	0.17
NE	3	178	21:18:50.051	+00:33:55.37	19.01	0.3132±0.0004	1	...	0.11
NW	1	25	21:18:46.617	+00:35:06.97	20.60	0.2727±0.0001	0	✓	0.41
NW	2	112	21:18:46.414	+00:34:26.28	20.33	0.2621±0.0001	0	...	0.26
NW	2	209	21:18:44.289	+00:33:42.58	19.24	0.2688±0.0001	0	✓	0.30
NW	3	161	21:18:42.244	+00:34:02.14	20.31	0.2735±0.0002	0	✓	0.44
NW	3	218	21:18:41.776	+00:33:36.44	19.08	0.1644±0.0001	0	...	0.31
SE	1	55	21:18:53.543	+00:33:18.15	18.90	0.2717±0.0001	0	✓	0.29
SE	1	185	21:18:53.214	+00:32:21.39	20.36	0.2774±0.0002	1	✓	0.42
SE	2	19	21:18:50.005	+00:33:26.22	19.07	0.2794±0.0002	0	✓	0.08
SE	2	24	21:18:52.466	+00:33:27.23	19.30	0.2786±0.0001	0	✓	0.22
SE	2	42	21:18:53.957	+00:33:21.27	19.97	0.2754±0.0001	0	✓	0.32
SE	2	155	21:18:52.670	+00:32:32.22	20.33	0.2132±0.0003	1	...	0.29
SE	3	56	21:18:54.097	+00:33:12.36	19.86	0.2284±0.0000	0	...	0.29
SW	1	100	21:18:47.781	+00:32:58.96	18.20	0.2276±0.0000	0	...	0.16
SW	1	120	21:18:43.405	+00:32:45.55	19.22	0.2811±0.0002	0	✓	0.42
SW	1	152	21:18:45.023	+00:32:33.46	18.62	0.2770±0.0001	0	✓	0.37
SW	1	167	21:18:45.081	+00:32:27.08	19.91	0.2786±0.0002	0	✓	0.39
SW	2	38	21:18:45.564	+00:33:22.07	20.54	0.3010±0.0001	1	...	0.24
SW	2	122	21:18:44.203	+00:32:45.66	20.29	0.2775±0.0001	0	✓	0.38
SW	2	206	21:18:42.699	+00:32:06.10	17.62	0.2700±0.0001	0	✓	0.55
SW	3	220	21:18:42.834	+00:31:57.86	21.05	0.2739±0.0000	0	✓	0.57

Table A.7: Spectroscopic redshifts for galaxies in c328p33+0p19 measured with the MS: m_r is the observed SDSS r magnitude. z is the derived redshift. Q is the redshift quality flag; see Section 3.4.1. Member? indicates whether the galaxy is a member of the cluster; see Section 3.4.2. See the appendix for similar tables for the remaining nine clusters.

tile	dither	fiber	ra	dec	r (mag)	redshift	Q	Member	R (Mp
NE	1	62	21:53:22.219	+00:12:39.81	20.97	0.0766±0.0001	1	...	0.10
NE	1	215	21:53:26.220	+00:11:40.21	16.71	0.2159±0.0001	0	✓	0.26
NE	2	138	21:53:23.595	+00:12:08.78	20.12	0.2737±0.0002	0	...	0.21
NE	2	220	21:53:21.347	+00:11:30.70	19.12	0.2192±0.0002	0	✓	0.00
NE	3	129	21:53:26.616	+00:12:12.42	19.97	0.2172±0.0002	0	✓	0.32
NE	3	154	21:53:24.770	+00:11:59.52	20.86	0.2809±0.0000	0	...	0.25
NE	3	168	21:53:24.545	+00:11:53.74	21.00	0.2210±0.0001	0	✓	0.19
NE	3	174	21:53:27.197	+00:11:53.68	19.85	0.2161±0.0001	0	✓	0.32
NW	1	206	21:53:15.345	+00:11:39.78	19.96	0.2170±0.0001	0	✓	0.32
NW	2	55	21:53:19.205	+00:12:46.30	20.20	0.2134±0.0002	0	✓	0.29
NW	3	151	21:53:16.776	+00:11:59.52	19.20	0.2166±0.0001	0	✓	0.26
NW	3	217	21:53:20.606	+00:11:34.95	20.71	0.2188±0.0002	1	✓	0.04
SE	1	12	21:53:26.058	+00:11:29.27	19.79	0.2164±0.0001	0	✓	0.25
SE	1	40	21:53:25.627	+00:11:16.34	18.96	0.2164±0.0001	0	✓	0.23
SE	3	43	21:53:27.012	+00:11:14.01	19.55	0.2159±0.0002	0	✓	0.30
SE	3	57	21:53:26.805	+00:11:06.27	19.54	0.2143±0.0001	0	✓	0.30
SE	3	61	21:53:21.720	+00:11:00.41	20.37	0.2144±0.0001	0	✓	0.11
SW	1	51	21:53:17.384	+00:11:10.44	19.13	0.2189±0.0001	0	✓	0.22
SW	1	174	21:53:20.933	+00:10:22.05	19.86	0.3719±0.0001	0	...	0.36
SW	2	133	21:53:14.825	+00:10:33.36	20.80	0.2085±0.0002	0	...	0.39
SW	3	41	21:53:19.548	+00:11:13.96	19.84	0.2138±0.0001	0	✓	0.11

Table A.8: Spectroscopic redshifts for galaxies in XMMXCSJ124425.9+164758.0 measured with the MS: m_r is the observed SDSS r magnitude. z is the derived redshift. Q is the redshift quality flag; see Section 3.4.1. Member? indicates whether the galaxy is a member of the cluster; see Section 3.4.2. See the appendix for similar tables for the remaining nine clusters.

tile	dither	fiber	ra	dec	r (mag)	redshift	Q	Member	R (Mp
NE	1	39	12:44:29.179	+16:49:17.17	19.38	0.4514±0.0001	0	...	0.61
NE	1	79	12:44:27.588	+16:48:59.30	20.00	0.2235±0.0001	1	...	0.29
NE	1	85	12:44:30.641	+16:48:58.51	19.65	0.2376±0.0001	0	...	0.40
NE	1	207	12:44:26.458	+16:48:01.70	20.04	0.2372±0.0002	1	...	0.09
NE	2	65	12:44:27.576	+16:49:04.52	20.86	0.2529±0.0001	1	...	0.33
NE	2	123	12:44:27.689	+16:48:39.78	18.94	0.1079±0.0001	1	...	0.12
NE	3	205	12:44:25.438	+16:48:00.39	18.15	0.2313±0.0002	0	✓	0.05
NW	1	17	12:44:23.999	+16:47:52.05	19.70	0.3377±0.0001	0	...	0.09
NW	1	70	12:44:28.565	+16:47:33.65	20.71	0.2372±0.0002	1	...	0.19
NW	2	6	12:44:25.438	+16:47:56.96	17.43	0.2340±0.0001	0	✓	0.04
NW	3	50	12:44:25.866	+16:47:35.40	20.14	0.2324±0.0002	0	✓	0.06
SE	1	164	12:44:27.304	+16:46:39.99	20.92	0.2302±0.0001	0	✓	0.27
SE	3	14	12:44:31.911	+16:47:47.15	19.72	0.4523±0.0001	0	...	0.56
SE	3	17	12:44:26.252	+16:47:41.10	20.39	0.2312±0.0000	0	✓	0.06
SE	3	105	12:44:26.799	+16:47:00.82	19.89	0.1361±0.0001	1	...	0.13
SW	1	25	12:44:23.322	+16:47:43.10	21.16	0.2192±0.0002	1	...	0.10
SW	1	29	12:44:25.243	+16:47:44.50	19.12	0.2316±0.0000	0	✓	0.01
SW	2	28	12:44:24.524	+16:47:42.65	17.24	0.0253±0.0001	1	...	0.01
SW	2	241	12:44:22.332	+16:46:07.60	18.90	0.2372±0.0001	0	...	0.41

Table A.9: Spectroscopic redshifts for galaxies in XMMXCSJ125650+254803.2 measured with the MS: m_r is the observed SDSS r magnitude. z is the derived redshift. Q is the redshift quality flag; see Section 3.4.1. Member? indicates whether the galaxy is a member of the cluster; see Section 3.4.2. See the appendix for similar tables for the remaining nine clusters.

tile	dither	fiber	ra	dec	r (mag)	redshift	Q	Member	R (Mp
NE	1	223	12:56:53.588	+25:48:02.73	19.64	0.3931±0.0001	1	...	0.26
NE	3	6	12:56:53.977	+25:49:31.89	18.33	0.1720±0.0001	0	...	0.30
NE	3	47	12:56:52.732	+25:49:10.94	18.32	0.1728±0.0001	0	...	0.23
NW	1	158	12:56:50.241	+25:48:32.88	19.07	0.2819±0.0001	0	✓	0.13
NW	1	170	12:56:49.017	+25:48:27.68	21.28	0.1665±0.0002	1	...	0.08
NW	3	201	12:56:50.112	+25:48:10.26	17.68	0.2810±0.0001	0	✓	0.03
SE	1	227	12:56:55.806	+25:46:22.69	19.95	0.3972±0.0001	1	...	0.68
SW	1	122	12:56:46.504	+25:47:04.28	19.49	0.3287±0.0001	0	...	0.36
SW	2	58	12:56:50.691	+25:47:36.32	19.90	0.2580±0.0001	0	...	0.11
SW	3	132	12:56:44.117	+25:46:56.15	18.06	0.2833±0.0001	0	✓	0.45
SW	3	138	12:56:47.249	+25:46:54.73	21.12	0.3280±0.0001	0	...	0.37

APPENDIX B

SECOND APPENDIX WITH A LONGER TITLE - MUCH LONGER IN FACT

Text for the Appendix follows.

Figure B.1: TAMU figure

B.1 Appendix Section